

Electronic Supplementary Information

From lithium to sodium: Design of heterometallic molecular precursors for the NaMO₂ cathode materials

Haixiang Han,^{a, c} Zheng Zhou,^a Jesse C. Carozza,^a Jeff Lengyel,^b Yuan Yao,^c Zheng Wei,^a
Evgeny V. Dikarev*^a

^a*Department of Chemistry, University at Albany, SUNY, Albany, NY, 12222, USA*

^b*Department of Chemistry and Biochemistry, Florida State University, FL 32306, USA*

^c*Department of Materials Science and Engineering, Cornell University, NY 14850, USA*

*Author to whom correspondence should be addressed. E-mail: edikarev@albany.edu. Phone:
(518)442-4401. Fax: (518)442-3462.

Table of Contents

Experimental Section. General Procedures.....	S1
Synthesis of Heterometallic Precursors	S3
X-ray Powder Diffraction Analysis of Heterometallic Precursors	S5
Crystal Growth.....	S9
X-ray Crystallographic Procedures.....	S10
Solid State Structures of Heterometallic Precursors.....	S13
ATR-IR Spectra of Heterometallic Precursors	S25
^1H NMR Investigation of Heterometallic Compound $\text{Na}_2\text{Mg}_2(\text{tbaoac})_6(\text{THF})_2$ (4).....	S27
DART Mass Spectra of Heterometallic Precursors	S28
Thermogravimetric Analysis (TGA) of Heterometallic Precursors.....	S38
Thermal Decomposition of Heterometallic Precursors.....	S39
TEM Image of Sodium Cobalt Oxide and Its Electrochemical Behavior	S44
References.....	S45

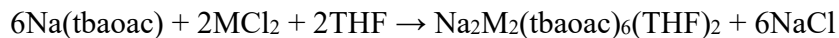
Experimental Section. General Procedures

All the manipulations were carried out in a dry, oxygen-free argon atmosphere by employing standard Schlenk and glove box techniques. Anhydrous iron(II) chloride (FeCl_2), cobalt(II) chloride (CoCl_2), nickel(II) chloride (NiCl_2), magnesium(II) chloride (MgCl_2), sodium methoxide (NaOMe), and *tert*-butyl acetoacetate (Htbaoc) were purchased from Sigma-Aldrich and used as received. The $\text{Fe}(\text{tbaoc})_2$, $\text{Co}(\text{tbaoc})_2$, $\text{Ni}(\text{tbaoc})_2$, and $\text{Mg}(\text{tbaoc})_2$ were prepared based on the reported synthetic procedures.¹⁻³ The attenuated total reflection (ATR) spectra were recorded on a PerkinElmer Spectrum 100FT-IR spectrometer. NMR spectra were obtained on a Bruker Advance 400 spectrometer at 400 MHz for ^1H . Chemical shifts (δ) are given in ppm relative to the residual solvent peaks. Mass spectra were acquired using a DART-SVP ion source (IonSense, Saugus, MA, USA) coupled to a JEOL AccuTOF time-of-flight mass spectrometer (JEOL USA, Peabody, MA, USA) in positive ion mode. Spectra were recorded over the mass range of m/z 50–2000 at one spectrum per second with a gas heater temperature of 300 °C. Thermogravimetric (TGA) measurements were carried out under air at a heating rate of 5 °C/min using a TGA 2050 Thermogravimetric Analyzer SDT Q600 V20.9 Build 20 Instruments. Thermal decomposition of heterometallic precursors was studied in air at ambient pressure. The solid sample (*ca.* 40 mg) was placed into a 20 mL Coors high-alumina crucible (Aldrich) and heated at a rate of *ca.* 35 °C/min in a muffle furnace (Lindberg Blue M). The decomposition residues were analyzed by X-ray powder diffraction. X-ray powder diffraction data were collected on a Bruker D8 Advance diffractometer (Cu $\text{K}\alpha$ radiation, focusing Göbel Mirror, LynxEye one-dimensional detector, step of 0.02° 2θ , 20 °C). The crystalline samples under investigation were ground and placed in the dome-like airtight zero-background holders. Le Bail fit for powder diffraction patterns has been performed using TOPAS, version 4 software package (Bruker AXS, 2006). Metal ratios were determined using inductively coupled plasma (ICP) analysis carried out on a Perkin-Elmer Optima 3300 DV ICP instrument. The samples were prepared by dissolving 10 mg of compound into 5 mL of highly concentrated nitric acid (68%) and diluting the resultant solution with deionized water to 100 mL. The samples for electron microscopy investigation were prepared by crushing the microcrystalline powder in a mortar in ethanol and depositing drops of suspension onto porous carbon grids. The electrochemical experiments were conducted on a Bio-Logic SP300 potentiostat. Three electrode set up was used with silver wire as reference electrode and Pt wire as the counter electrode. 1 molar sodium perchlorate in acetonitrile solution was employed as the electrolyte. For

cyclic voltammetry, the scan range was between -1.5-0.5 V at a scan speed of 5 mV/s. For the galvanostatic charge/discharge experiments, the voltage scan was performed from -1.5 to 0.5 V at the rate of C/20.

Synthesis of Heterometallic Precursors

Method I



A flask was charged with a mixture of MCl_2 ($\text{M} = \text{Fe, Co, Ni, Mg}$) and Na(tbaooac) under dry argon atmosphere, and 100 mL of dry, deoxygenated THF was added. The solution was stirred at room temperature for 3 days. The NaCl was filtered off before evaporating the solvent under vacuum at room temperature. The residue was dried under vacuum at room temperature overnight. No further purification was necessary. The purity of the solid residues was confirmed by X-ray powder diffraction analysis (Figures S1–S4, Tables S4–S7). Experimental details are summarized in Table S1.

Table S1. Experimental Details for the Synthesis of Heterometallic Precursors $\text{Na}_2\text{M}_2(\text{tbaooac})_6(\text{THF})_2$ ($\text{M} = \text{Fe (1), Co (2), Ni (3), and Mg (4)}$)

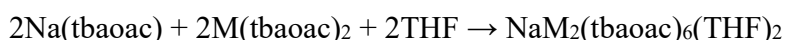
Compound	1	2	3	4
MCl_2 (g, mmol)	0.100, 0.789	0.100, 0.770	0.100, 0.772	0.100, 1.05
Na(tbaooac) (g, mmol)	0.426, 2.37	0.416, 2.31	0.417, 2.32	0.568, 3.15
Yield (g)	0.446	0.448	0.444	0.583
Yield (%)	91	93	92	94
Color	Orange	Pink	Green	Colorless

Compound $\text{Na}_2\text{Fe}_2(\text{tbaooac})_6(\text{THF})_2$ (**1**) can also be obtained by slightly different procedure. A flask was charged with a mixture of FeCl_2 and Na(tbaooac) under dry argon atmosphere, and 100 mL of dry, deoxygenated acetone was added. The solution was stirred at room temperature for 1 hour. The NaCl solid was then filtered off, and the solvent was evaporated under vacuum. The residue was dried further by heating at 100 °C under vacuum overnight. The dried solid residue was redissolved in the in 50 mL of dry, deoxygenated THF. The solution was stirred for 30 minutes or until all solid was dissolved. The solvent was evaporated under vacuum, and the final product was further dried under vacuum at room temperature overnight. Experimental details are summarized in Table S2.

Table S2. Experimental Details for the Synthesis of Heterometallic Precursor Na₂Fe₂(tbaoac)₆(THF)₂ (**1**)

Compound	1
FeCl ₂ (g, mmol)	0.100, 0.789
Na(tbaoac) (g, mmol)	0.426, 2.37
Yield (g)	0.444
Yield (%)	91
Color	Orange

Method II



A flask was charged with a mixture of Na(tbaoac) and M(tbaoac)₂ under dry argon atmosphere and 50 mL of dry, deoxygenated THF was added. The solution was stirred at room temperature for 1 hour. The solvent was evaporated under vacuum at room temperature, and the final product was further dried under vacuum at room temperature overnight. Experimental details are summarized in Table S3.

Table S3. Experimental Details for the Synthesis of Heterometallic Precursors Na₂M₂(tbaoac)₆(THF)₂ (M = Fe (**1**), Co (**2**), Ni (**3**), and Mg (**4**))

Compound	1	2	3	4
M(tbaoac) ₂ (g, mmol)	1.027, 2.77	1.036, 2.78	1.035, 2.77	0.940, 2.78
Na(tbaoac) (g, mmol)	0.500, 2.78	0.500, 2.78	0.500, 2.78	0.500, 2.78
Time (hours)	1	1	1	1
Yield (g)	1.262	1.597	1.579	1.525
Yield (%)	91	92	91	93
Color	Orange	Pink	Green	Colorless

X-ray Powder Diffraction Analysis of Heterometallic Precursors

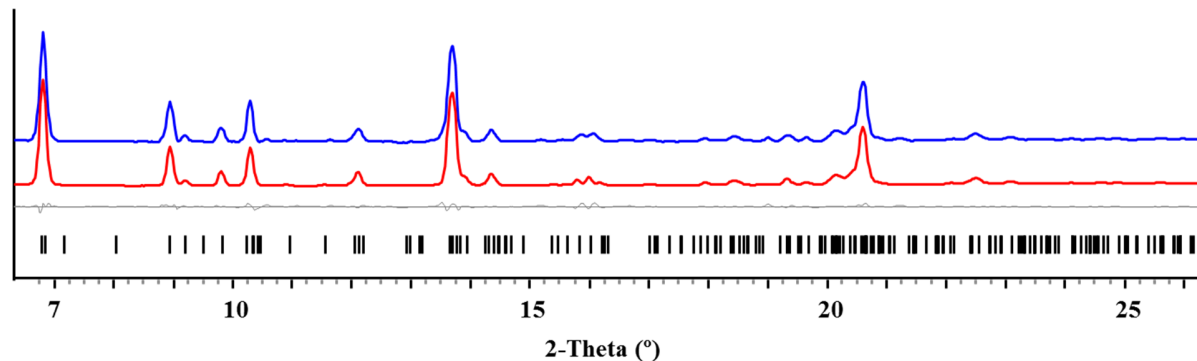


Figure S1. X-ray powder pattern of $\text{Na}_2\text{Fe}_2(\text{tbaoac})_6(\text{THF})_2$ (**1**) and the Le Bail fit. Blue and red curves are experimental and calculated patterns, respectively. Grey line is the difference curve with theoretical peak positions shown at the bottom.

Table S4. Unit Cell Parameters for $\text{Na}_2\text{Fe}_2(\text{tbaoac})_6(\text{THF})_2$ (**1**) Obtained by the Le Bail Fit and from the Single Crystal Data

Na ₂ Fe ₂ (tbaoac) ₆ (THF) ₂ (1)		
	Le Bail fit (20 °C)	Single Crystal (-173 °C)
Sp. Gr.		P-1
<i>a</i> (Å)	10.025(1)	9.9939(8)
<i>b</i> (Å)	13.935(1)	13.6299(12)
<i>c</i> (Å)	25.901(1)	25.8470(23)
α (°)	96.571(3)	96.862(2)
β (°)	92.682(3)	92.122(2)
γ (°)	106.591(2)	106.890(2)
<i>V</i> (Å ³)	3432.9(8)	3335.22(?)

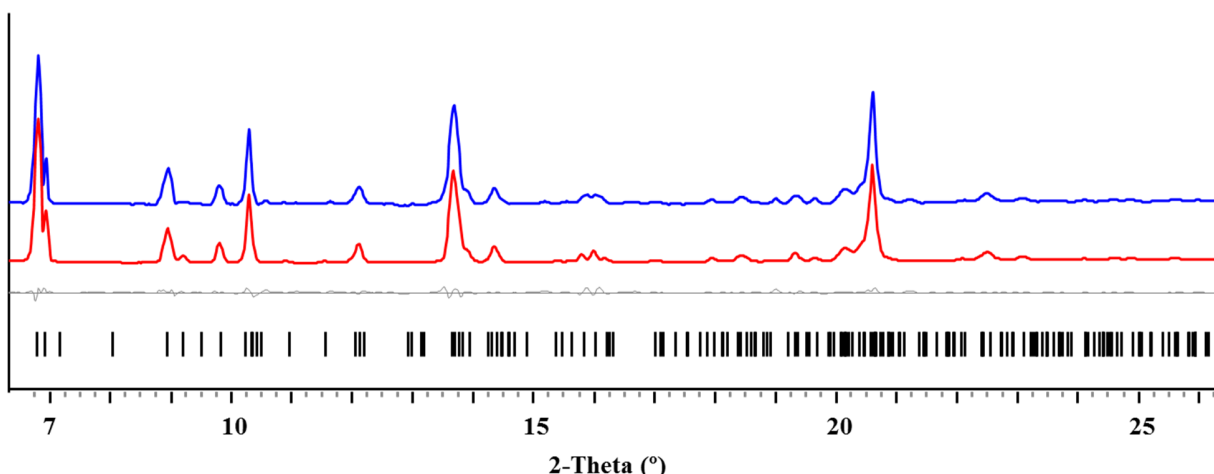


Figure S2. X-ray powder pattern of $\text{Na}_2\text{Co}_2(\text{tbaoac})_6(\text{THF})_2$ (**2**) and the Le Bail fit. Blue and red curves are experimental and calculated patterns, respectively. Grey line is the difference curve with theoretical peak positions shown at the bottom.

Table S5. Unit Cell Parameters for $\text{Na}_2\text{Co}_2(\text{tbaoac})_6(\text{THF})_2$ (**2**) Obtained by the Le Bail Fit and from the Single Crystal Data

Na ₂ Co ₂ (tbaoac) ₆ (THF) ₂ (2)		
	Le Bail fit (20 °C)	Single Crystal (-173 °C)
Sp. Gr.		<i>P</i> -1
<i>a</i> (Å)	9.9411(5)	9.9404(11)
<i>b</i> (Å)	13.8428(5)	13.6413(16)
<i>c</i> (Å)	25.7882(5)	25.787(3)
α (°)	96.424(3)	96.319(3)
β (°)	92.369(3)	92.385(3)
γ (°)	106.928(4)	106.847(3)
<i>V</i> (Å ³)	3368.76(8)	3316.4(7)

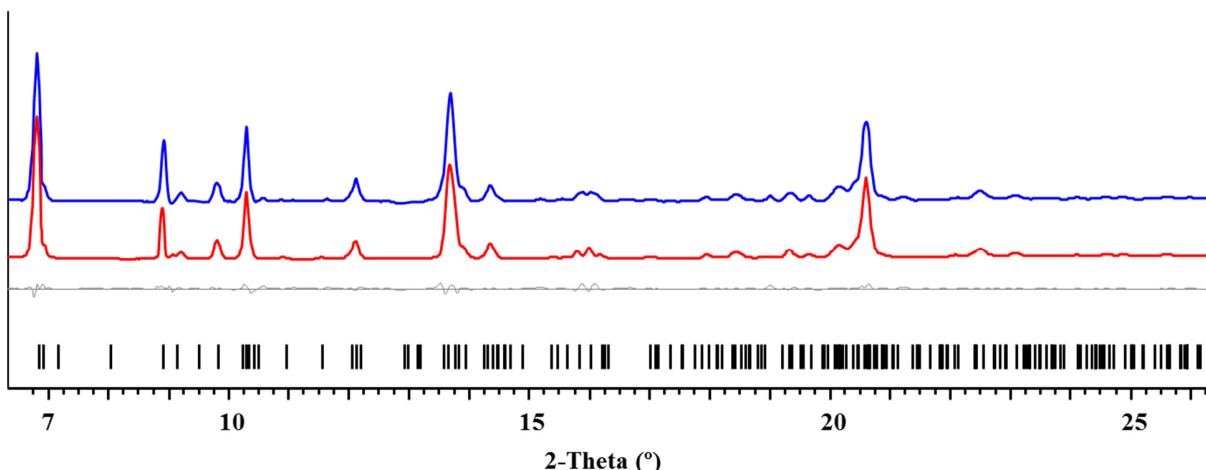


Figure S3. X-ray powder pattern of $\text{Na}_2\text{Ni}_2(\text{tbaoac})_6(\text{THF})_2$ (**3**) and the Le Bail fit. Blue and red curves are experimental and calculated patterns, respectively. Grey line is the difference curve with theoretical peak positions shown at the bottom.

Table S6. Unit Cell Parameters for $\text{Na}_2\text{Ni}_2(\text{tbaoac})_6(\text{THF})_2$ (**3**) Obtained by the Le Bail Fit and from the Single Crystal Data

Na ₂ Ni ₂ (tbaoac) ₆ (THF) ₂ (3)		
	Le Bail fit (20 °C)	Single Crystal (-173 °C)
Sp. Gr.		<i>P</i> -1
<i>a</i> (Å)	9.9185(8)	9.9084(11)
<i>b</i> (Å)	13.7368(8)	13.7071(16)
<i>c</i> (Å)	25.7204(8)	25.702(3)
α (°)	96.392(5)	96.380(3)
β (°)	92.547(5)	92.531(3)
γ (°)	106.969(5)	106.949(3)
<i>V</i> (Å ³)	3320.1(7)	3307.6(7)

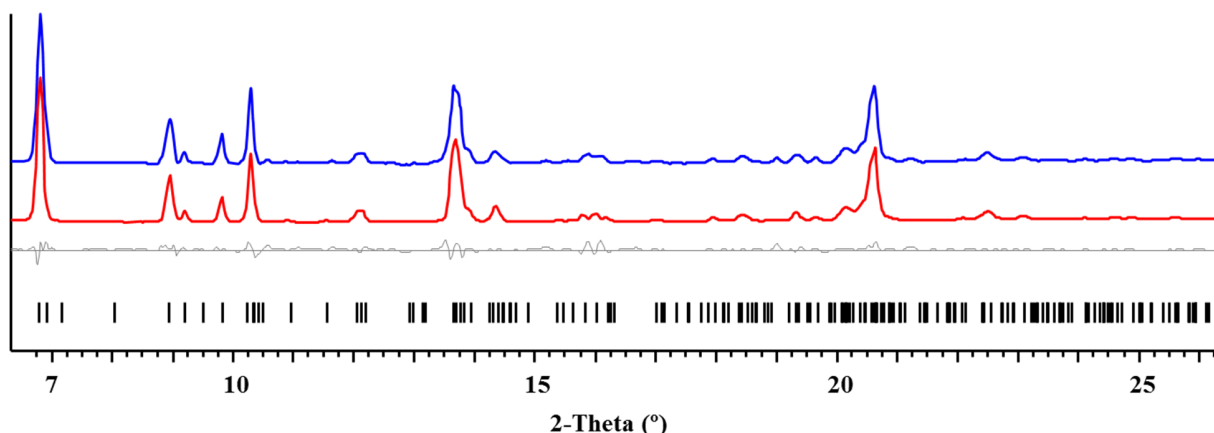


Figure S4. X-ray powder pattern of $\text{Na}_2\text{Mg}_2(\text{tbaoac})_6(\text{THF})_2$ (**4**) and the Le Bail fit. Blue and red curves are experimental and calculated patterns, respectively. Grey line is the difference curve with theoretical peak positions shown at the bottom.

Table S7. Unit Cell Parameters for $\text{Na}_2\text{Mg}_2(\text{tbaoac})_6(\text{THF})_2$ (**4**) Obtained by the Le Bail Fit and from the Single Crystal Data

Na ₂ Mg ₂ (tbaoac) ₆ (THF) ₂ (4)		
	Le Bail fit (20 °C)	Single Crystal (-173 °C)
Sp. Gr.		<i>P</i> -1
<i>a</i> (Å)	9.9601(8)	9.9586(4)
<i>b</i> (Å)	13.7014(8)	13.6982(5)
<i>c</i> (Å)	25.8311(7)	25.8204(10)
α (°)	96.604(8)	96.573(2)
β (°)	92.230(6)	92.247(2)
γ (°)	106.925(6)	107.056(2)
<i>V</i> (Å ³)	3340.4(8)	3335.4(2)

Crystal Growth

Rod-shaped crystals of $\text{Na}_2\text{M}_2(\text{tbaoac})_6(\text{THF})_2$ ($\text{M} = \text{Fe}$ (**1**), Co (**2**), Ni (**3**), and Mg (**4**)) suitable for X-ray single crystal structural measurements were obtained by slow evaporation method, in which saturated solutions of **1-4** in dry, degassed THF were sealed in “L-shaped” glass ampules under reduced-pressure argon atmosphere. The solution-containing end of the ampule was placed above a heating sand bath with the temperature about 3-5 °C higher than the room temperature and was kept for several days to promote optimal crystal growth.

Table S8. Single Crystal Growth Conditions

Compound	1	2	3	4
Shape	Rod	Rod	Rod	Rod
Color	Orange	Pink	Green	Colorless
Crystal Growth Method	Slow evaporation of THF solution			
Temperature (°C)	Room temperature			
Time (days)	5	3	3	3

X-ray Crystallographic Procedures

The single crystal diffraction data for **1**, **2** and **3** were measured on a Bruker D8 VENTURE diffractometer with PHOTON 100 CMOS shutterless mode detector system equipped with a sealed Mo-target X-ray tube ($\lambda = 0.71073 \text{ \AA}$). The single crystal diffraction data for **4** were measured on the same diffractometer with a Cu-target, $1\mu\text{S}$ microfocus X-ray tube ($\lambda = 1.54178 \text{ \AA}$). All data reduction and integration were performed with the Bruker software package SAINT (version 8.34A).⁴ Data were corrected for absorption effects using the empirical methods as implemented in SADABS (version 2016/2).⁵ The structures were solved by SHELXT (version 2018/2)⁶ and refined by full-matrix least-squares procedures using the SHELXTL (version 2018/3)⁷ through the OLEX2⁸ graphical interface. All non-hydrogen atoms, including those in disordered parts, were refined anisotropically. All hydrogen atoms were included in idealized positions for structure factor calculations with $U_{\text{iso}}(\text{H}) = 1.2 \cdot U_{\text{eq}}(\text{C})$ for *tert*-butyl groups and $U_{\text{iso}}(\text{H}) = 1.5 \cdot U_{\text{eq}}(\text{C})$ for methyl groups. All disordered groups were modelled with two orientations using similarity restraints (SAME command in SHELXL). The anisotropic displacement parameters of the disordered THF molecules in the direction of the bonds were restrained to be equal with a standard uncertainty of 0.01 \AA^2 . They were also restrained to have the same U_{ij} components, with a standard uncertainty of 0.04 \AA^2 . Crystallographic data, details of the data collection and structure refinement parameters for compounds **1-4** are listed in Table S9.

Table S9. Crystal Data and Structure Refinement Parameters for $\text{Na}_2\text{Fe}_2(\text{tbaoac})_6(\text{THF})_2$ (**1**), $\text{Na}_2\text{Co}_2(\text{tbaoac})_6(\text{THF})_2$ (**2**), $\text{Na}_2\text{Ni}_2(\text{tbaoac})_6(\text{THF})_2$ (**3**), and $\text{Na}_2\text{Mg}_2(\text{tbaoac})_6(\text{THF})_2$ (**4**)

Compound	1	2	3
Empirical formula	$\text{C}_{56}\text{H}_{94}\text{Fe}_2\text{Na}_2\text{O}_{20}$	$\text{C}_{56}\text{H}_{94}\text{Co}_2\text{Na}_2\text{O}_{20}$	$\text{C}_{56}\text{H}_{94}\text{Ni}_2\text{Na}_2\text{O}_{20}$
Formula weight	1244.99	1251.15	1250.71
Temperature (K)	100(2)	100(2)	100(2)
Wavelength (Å)	0.71073	0.71073	0.71073
Crystal system	triclinic	triclinic	triclinic
Space group	<i>P</i> -1	<i>P</i> -1	<i>P</i> -1
<i>a</i> (Å)	9.9939(8)	9.9404(11)	9.9084(11)
<i>b</i> (Å)	13.6299(12)	13.6413(16)	13.7071(16)
<i>c</i> (Å)	25.847(2)	25.787(3)	25.702(3)
α (°)	96.862(2)	96.319(3)	96.380(3)
β (°)	92.122(2)	92.385(3)	92.531(3)
γ (°)	106.890(2)	106.847(3)	106.949(3)
<i>V</i> (Å ³)	3335.2(5)	3316.4(7)	3307.6(7)
<i>Z</i>	2	2	2
ρ_{calcd} (g·cm ⁻³)	1.240	1.253	1.256
μ (mm ⁻¹)	0.514	0.579	0.648
<i>F</i> (000)	1328	1332	1336
Crystal size (mm)	0.40x0.03x0.01	0.30x0.040x0.020	0.60x0.02x0.02
θ range (°)	3.009-25.000	2.781-24.999	2.782-24.999
Reflections collected	119522	82996	93101
Independent reflections	11723	11654	11625
	[$R_{\text{int}} = 0.0435$]	[$R_{\text{int}} = 0.0830$]	[$R_{\text{int}} = 0.0702$]
Transmission factors	0.9221/1	0.9358/1	0.9210/1
(min/max)			
Data/restr/params	11723/578/868	11654/572/868	11625/572/868
<i>R</i> 1, ^a <i>wR</i> 2 ^b (<i>I</i> > 2σ(<i>I</i>))	0.0323, 0.0667	0.0441, 0.0737	0.0394, 0.0697
<i>R</i> 1, ^a <i>wR</i> 2 ^b (all data)	0.0493, 0.0739	0.0914, 0.0877	0.0716, 0.0796
Quality-of-fit ^c	1.025	1.010	1.021
Largest diff. peak and hole (e·Å ⁻³)	0.0337 and -0.207	0.313 and -0.289	0.312 and -0.244

^a $R1 = \sum ||F_o|| - |F_c|| / \sum |F_o|$. ^b $wR2 = [\sum [w(F_o^2 - F_c^2)^2] / \sum [w(F_o^2)^2]]$.

^cQuality-of-fit = $[\sum [w(F_o^2 - F_c^2)^2] / (N_{\text{obs}} - N_{\text{params}})]^{1/2}$, based on all data.

Table S9. (*Cont'd*)

Compound	4
Empirical formula	C ₅₆ H ₉₄ Mg ₂ Na ₂ O ₂₀
Formula weight	1181.91
Temperature (K)	100(2)
Wavelength (Å)	1.54178
Crystal system	triclinic
Space group	<i>P</i> -1
<i>a</i> (Å)	9.9586(4)
<i>b</i> (Å)	13.6982(5)
<i>c</i> (Å)	25.8204(10)
α (°)	96.573(2)
β (°)	92.247(2)
γ (°)	107.056(2)
<i>V</i> (Å ³)	3335.4(2)
<i>Z</i>	2
ρ_{calcd} (g·cm ⁻³)	1.177
μ (mm ⁻¹)	1.000
<i>F</i> (000)	1272
Crystal size (mm)	0.500x0.040x0.030
θ range (°)	3.404-66.998
Reflections collected	68924
Independent reflections	11740
	[$R_{\text{int}} = 0.1269$]
Transmission factors (min/max)	0.8612/1
Data/restr/params	11740/578/868
<i>R</i> 1, ^a <i>wR</i> 2 ^b (<i>I</i> > 2 σ (<i>I</i>))	0.0466, 0.0989
<i>R</i> 1, ^a <i>wR</i> 2 ^b (all data)	0.0866, 0.1166
Quality-of-fit ^c	1.010
Largest diff. peak and hole (e ⁻ ·Å ⁻³)	0.204 and -0.217

^a $R_1 = \sum ||F_o|| - |F_c|| / \sum |F_o|$. ^b $wR2 = [\sum [w(F_o^2 - F_c^2)^2] / \sum [w(F_o^2)^2]]$.

^cQuality-of-fit = $[\sum [w(F_o^2 - F_c^2)^2] / (N_{\text{obs}} - N_{\text{params}})]^{1/2}$, based on all data.

Solid State Structures of Heterometallic Precursors

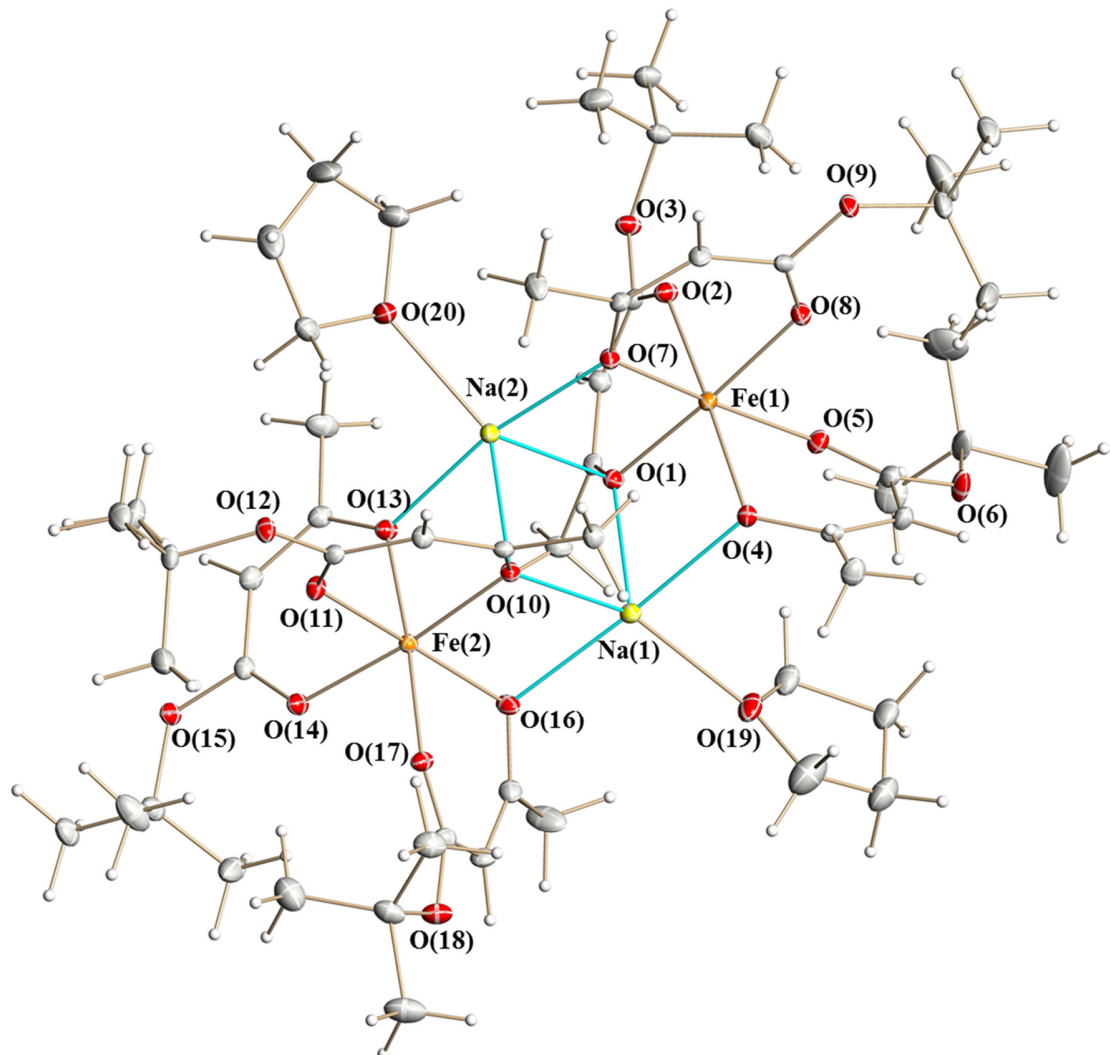


Figure S5. Solid state structure of heterometallic complex $\text{Na}_2\text{Fe}_2(\text{tbaoac})_6(\text{THF})_2$ (**1**) drawn with thermal ellipsoids at the 40% probability level. Hydrogen atoms are represented by spheres of arbitrary radius. Only metal and oxygen atoms are labeled. The sodium–oxygen bonds to the tbaoac ligands involved in bridging interactions are shown in blue.

Table S10. Selected Bond Distances (\AA) and Angles ($^\circ$) in the Structure of $\text{Na}_2\text{Fe}_2(\text{tbaoac})_2(\text{THF})_2$ (1)

Bond distances					
Fe(1)–O(1)**	2.1157(12)	Fe(2)–O(10)**	2.0978(12)	Na(1)–O(1)*	2.3859(14)
Fe(1)–O(2)	2.0984(12)	Fe(2)–O(11)	2.0950(13)	Na(1)–O(4)*	2.3530(14)
Fe(1)–O(4)**	2.0697(13)	Fe(2)–O(13)**	2.0690(12)	Na(1)–O(10)*	2.3475(14)
Fe(1)–O(5)	2.1135(12)	Fe(2)–O(14)	2.0958(12)	Na(1)–O(16)*	2.3888(14)
Fe(1)–O(7)**	2.0763(12)	Fe(2)–O(16)**	2.0783(13)	Na(1)–O(19)	2.359(15)
Fe(1)–O(8)	2.0876(12)	Fe(2)–O(17)	2.1261(13)		
Na(2)–O(1)*	2.4347(14)				
Na(2)–O(7)*	2.2828(14)				
Na(2)–O(10)*	2.4073(14)				
Na(2)–O(13)*	2.2851(14)				
Na(2)–O(20)	2.366(11)				
Angles					
O(2)–Fe(1)–O(1)	85.12(5)	O(10)–Fe(2)–O(17)	91.78(5)	O(1)–Na(1)–O(16)	97.50(5)
O(2)–Fe(1)–O(5)	89.94(5)	O(11)–Fe(2)–O(10)	84.75(5)	O(4)–Na(1)–O(1)	78.12(5)
O(4)–Fe(1)–O(1)	91.04(5)	O(11)–Fe(2)–O(14)	90.65(5)	O(4)–Na(1)–O(16)	175.62(5)
O(4)–Fe(1)–O(2)	173.06(5)	O(11)–Fe(2)–O(17)	94.49(5)	O(10)–Na(1)–O(1)	93.34(5)
O(4)–Fe(1)–O(5)	84.45(5)	O(13)–Fe(2)–O(10)	93.11(5)	O(10)–Na(1)–O(4)	102.14(5)
O(4)–Fe(2)–O(7)	96.73(5)	O(13)–Fe(2)–O(11)	87.94(5)	O(10)–Na(1)–O(16)	77.99(5)
O(4)–Fe(1)–O(8)	94.89(5)	O(13)–Fe(2)–O(14)	87.45(5)	O(10)–Na(1)–O(19)	113.1(4)
O(5)–Fe(1)–O(1)	92.55(5)	O(13)–Fe(2)–O(16)	94.66(5)	O(19)–Na(1)–O(1)	152.0(4)
O(7)–Fe(1)–O(1)	91.25(5)	O(13)–Fe(2)–O(17)	174.72(5)	O(19)–Na(1)–O(4)	87.0(5)
O(7)–Fe(1)–O(2)	89.14(5)	O(14)–Fe(2)–O(10)	175.34(5)	O(19)–Na(1)–O(16)	97.0(5)
O(7)–Fe(1)–O(5)	176.00(5)	O(14)–Fe(2)–O(17)	87.84(5)		
O(7)–Fe(1)–O(8)	86.44(5)	O(16)–Fe(2)–O(10)	91.07(5)		
O(8)–Fe(1)–O(1)	173.85(5)	O(16)–Fe(2)–O(11)	175.20(5)		
O(8)–Fe(1)–O(2)	89.14(5)	O(16)–Fe(2)–O(14)	93.49(5)		
O(8)–Fe(1)–O(5)	89.66(5)	O(16)–Fe(2)–O(17)	83.25(5)		

* – bridging oxygen; ** – chelating-bridging oxygen

Angles	
O(7)–Na(2)–O(1)	78.79(5)
O(7)–Na(2)–O(10)	93.47(5)
O(7)–Na(2)–O(13)	170.00(5)
O(7)–Na(2)–O(20)	95.2(6)
O(10)–Na(2)–O(1)	90.65(5)
O(13)–Na(2)–O(1)	93.41(5)
O(13)–Na(2)–O(10)	80.25(5)
O(13)–Na(2)–O(20)	94.6(6)
O(20)–Na(2)–O(1)	129.0(5)
O(20)–Na(2)–O(10)	140.3(5)

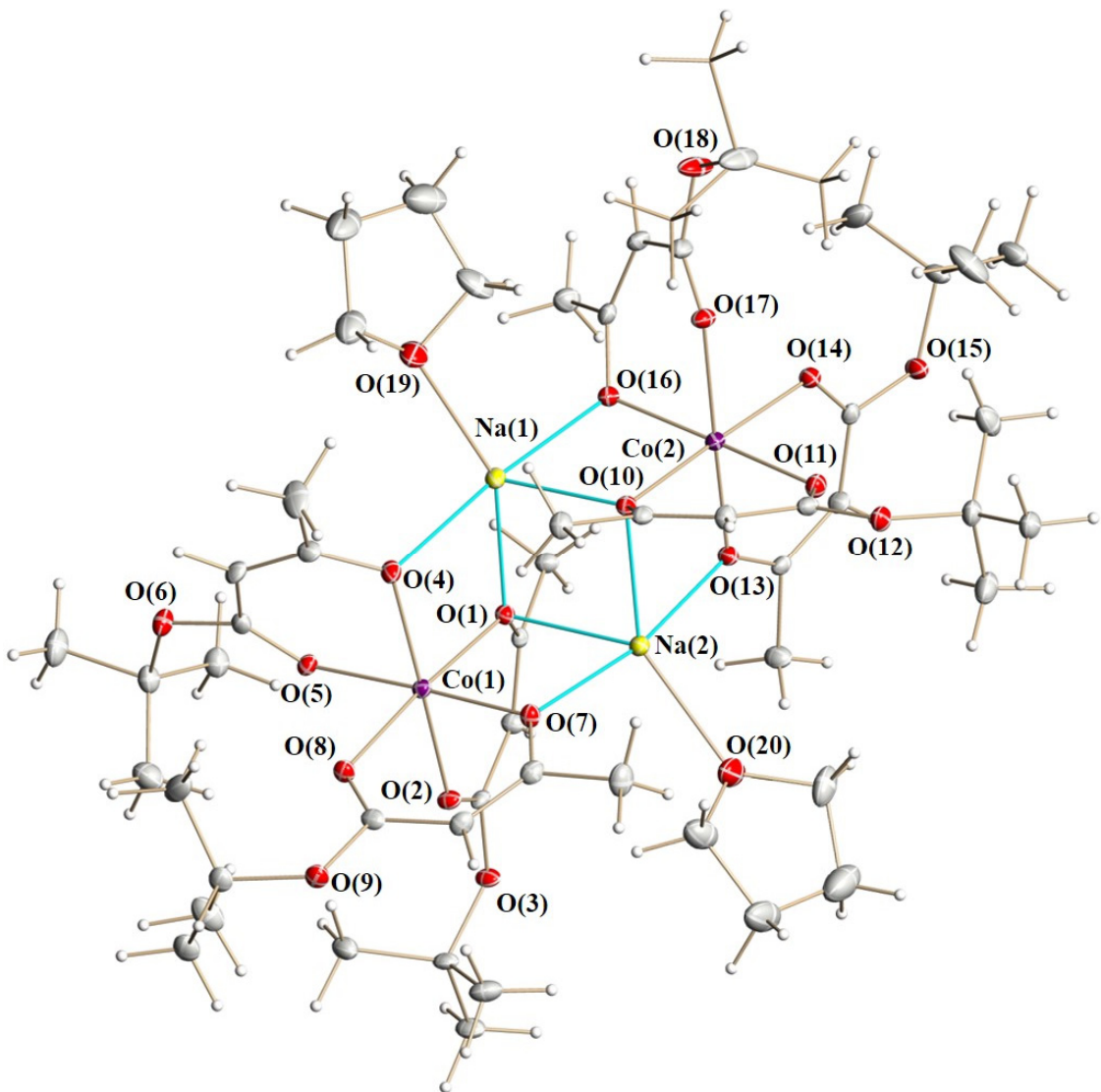


Figure S6. Solid state structure of heterometallic complex $\text{Na}_2\text{Co}_2(\text{tbaoac})_6(\text{THF})_2$ (**2**) drawn with thermal ellipsoids at the 40% probability level. Hydrogen atoms are represented by spheres of arbitrary radius. Only metal and oxygen atoms are labeled. The sodium–oxygen bonds to the tbaoac ligands involved in bridging interactions are shown in blue.

Table S11. Selected Bond Distances (Å) and Angles (°) in the Structure of $\text{Na}_2\text{Co}_2(\text{tbaoac})_2(\text{THF})_2$ (2)

Bond distances				
Co(1)–O(1)**	2.1064(17)	Co(2)–O(10)**	2.0902(18)	Na(1)–O(1)*
Co(1)–O(2)	2.0582(18)	Co(2)–O(11)	2.0575(19)	Na(1)–O(4)*
Co(1)–O(4)**	2.0399(18)	Co(2)–O(13)**	2.0401(18)	Na(1)–O(10)*
Co(1)–O(5)	2.0887(18)	Co(2)–O(14)	2.0655(18)	Na(1)–O(16)*
Co(1)–O(7)**	2.0462(18)	Co(2)–O(16)**	2.0420(18)	Na(1)–O(19)
Co(1)–O(8)	2.0634(18)	Co(2)–O(17)	2.0997(18)	
Na(2)–O(1)*	2.428(2)			
Na(2)–O(7)*	2.272(2)			
Na(2)–O(10)*	2.391(2)			
Na(2)–O(13)*	2.264(2)			
Na(2)–O(20)	2.339(15)			
Angles				
O(2)–Co(1)–O(1)	87.01(7)	O(10)–Co(2)–O(17)	91.87(7)	O(1)–Na(1)–O(16)
O(2)–Co(1)–O(5)	89.01(7)	O(11)–Co(2)–O(10)	86.66(7)	O(4)–Na(1)–O(1)
O(2)–Co(1)–O(8)	88.14(7)	O(11)–Co(2)–O(14)	89.31(7)	O(4)–Na(1)–O(16)
O(4)–Co(1)–O(1)	89.48(7)	O(11)–Co(2)–O(17)	92.17(7)	O(4)–Na(1)–O(19)
O(4)–Co(1)–O(2)	174.22(7)	O(13)–Co(2)–O(10)	91.05(7)	O(10)–Na(1)–O(1)
O(4)–Co(1)–O(5)	86.60(7)	O(13)–Co(2)–O(11)	89.47(7)	O(10)–Na(1)–O(4)
O(4)–Co(1)–O(7)	93.63(7)	O(13)–Co(2)–O(14)	90.26(7)	O(10)–Na(1)–O(16)
O(4)–Co(1)–O(8)	95.43(7)	O(13)–Co(2)–O(16)	92.92(7)	O(10)–Na(1)–O(19)
O(5)–Co(1)–O(1)	93.11(7)	O(13)–Co(2)–O(17)	176.73(7)	O(19)–Na(1)–O(1)
O(7)–Co(1)–O(1)	89.74(7)	O(14)–Co(2)–O(10)	175.74(7)	O(19)–Na(1)–O(16)
O(7)–Co(1)–O(2)	90.95(7)	O(14)–Co(2)–O(17)	86.93(7)	
O(7)–Co(1)–O(5)	177.15(7)	O(16)–Co(2)–O(10)	89.49(7)	
O(7)–Co(1)–O(8)	89.43(7)	O(16)–Co(2)–O(11)	175.51(7)	
O(8)–Co(1)–O(1)	175.07(7)	O(16)–Co(2)–O(14)	94.49(7)	
O(8)–Co(1)–O(5)	87.72(7)	O(16)–Co(2)–O(17)	85.64(7)	

* – bridging oxygen; ** – chelating-bridging oxygen

Angles	
O(7)–Na(2)–O(1)	77.06(7)
O(7)–Na(2)–O(10)	94.85(7)
O(7)–Na(2)–O(20)	94.0(10)
O(10)–Na(2)–O(1)	91.40(7)
O(13)–Na(2)–O(1)	94.29(7)
O(13)–Na(2)–O(7)	169.07(8)
O(13)–Na(2)–O(10)	78.52(7)
O(13)–Na(2)–O(20)	96.7(11)
O(20)–Na(2)–O(1)	128.5(7)
O(20)–Na(2)–O(10)	140.1(7)

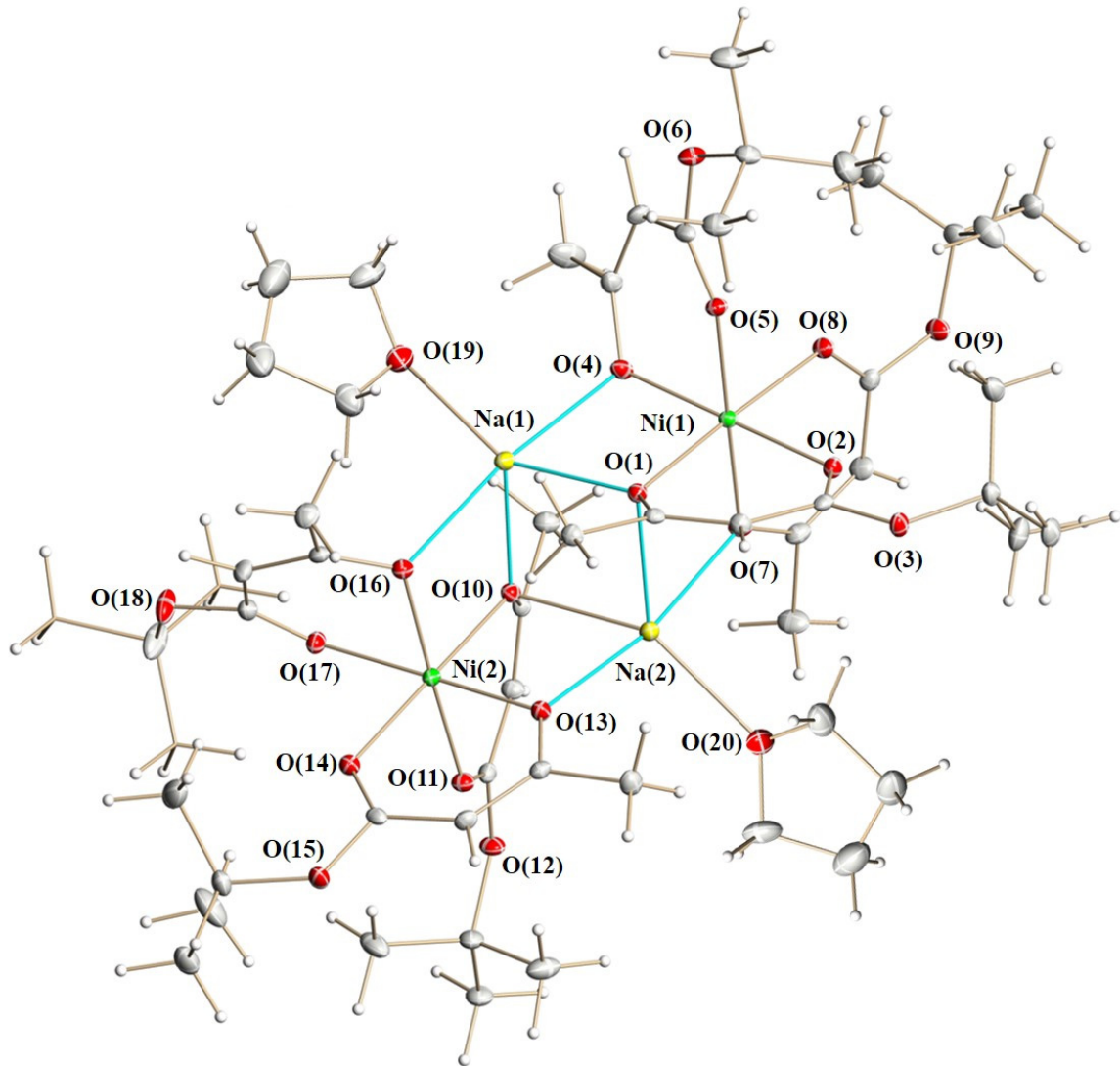


Figure S7. Solid state structure of heterometallic complex $\text{Na}_2\text{Ni}_2(\text{tbaoac})_6(\text{THF})_2$ (**3**) drawn with thermal ellipsoids at the 40% probability level. Hydrogen atoms are represented by spheres of arbitrary radius. Only metal and oxygen atoms are labeled. The sodium–oxygen bonds to the tbaoac ligands involved in bridging interactions are shown in blue.

Table S12. Selected Bond Distances (\AA) and Angles ($^\circ$) in the Structure of $\text{Na}_2\text{Ni}_2(\text{tbaoac})_2(\text{THF})_2$ (3)

Bond distances					
Ni(1)–O(1)**	2.0583(15)	Ni(2)–O(10)**	2.0465(15)	Na(1)–O(1)*	2.3452(18)
Ni(1)–O(2)	2.0312(16)	Ni(2)–O(11)	2.0305(16)	Na(1)–O(4)*	2.3742(18)
Ni(1)–O(4)**	2.0207(16)	Ni(2)–O(13)**	2.0145(16)	Na(1)–O(10)*	2.3248(18)
Ni(1)–O(5)	2.0456(16)	Ni(2)–O(14)	2.0331(16)	Na(1)–O(16)*	2.4071(18)
Ni(1)–O(7)**	2.0182(16)	Ni(2)–O(16)**	2.0270(16)	Na(1)–O(19)	2.317(12)
Ni(1)–O(8)	2.0301(15)	Ni(2)–O(17)	2.0579(16)		
Na(2)–O(1)*	2.4456(18)				
Na(2)–O(7)*	2.2546(18)				
Na(2)–O(10)*	2.4032(18)				
Na(2)–O(13)*	2.2506(18)				
Na(2)–O(20)	2.341(16)				
Angles					
O(2)–Ni(1)–O(1)	89.14(6)	O(10)–Ni(2)–O(17)	91.10(6)	O(1)–Na(1)–O(4)	75.17(6)
O(2)–Ni(1)–O(5)	90.25(6)	O(11)–Ni(2)–O(10)	88.72(6)	O(1)–Na(1)–O(16)	98.27(6)
O(4)–Ni(1)–O(1)	89.76(6)	O(11)–Ni(2)–O(14)	88.42(6)	O(4)–Na(1)–O(16)	172.09(7)
O(4)–Ni(1)–O(2)	178.35(7)	O(11)–Ni(2)–O(17)	92.63(7)	O(10)–Na(1)–O(1)	96.12(6)
O(4)–Ni(1)–O(5)	88.55(6)	O(13)–Ni(2)–O(10)	91.03(6)	O(10)–Na(1)–O(4)	101.55(6)
O(4)–Ni(1)–O(8)	93.63(6)	O(13)–Ni(2)–O(11)	89.04(7)	O(10)–Na(1)–O(16)	74.46(6)
O(5)–Ni(1)–O(1)	91.62(6)	O(13)–Ni(2)–O(14)	91.23(6)	O(10)–Na(1)–O(19)	112.5(3)
O(7)–Ni(1)–O(1)	89.77(6)	O(13)–Ni(2)–O(16)	90.97(6)	O(19)–Na(1)–O(1)	150.1(3)
O(7)–Ni(1)–O(2)	90.43(6)	O(13)–Ni(2)–O(17)	177.32(7)	O(19)–Na(1)–O(4)	90.2(6)
O(7)–Ni(1)–O(4)	90.80(7)	O(14)–Ni(2)–O(10)	176.33(6)	O(19)–Na(1)–O(16)	97.6(6)
O(7)–Ni(1)–O(5)	178.45(6)	O(14)–Ni(2)–O(17)	86.73(6)		
O(7)–Ni(1)–O(8)	90.69(6)	O(16)–Ni(2)–O(10)	89.33(6)		
O(8)–Ni(1)–O(1)	176.57(6)	O(16)–Ni(2)–O(11)	178.04(6)		
O(8)–Ni(1)–O(2)	87.46(6)	O(16)–Ni(2)–O(14)	93.54(6)		
O(8)–Ni(1)–O(5)	87.95(6)	O(16)–Ni(2)–O(17)	87.42(6)		

* – bridging oxygen; ** – chelating-bridging oxygen

Angles	
O(7)–Na(2)–O(1)	75.36(6)
O(7)–Na(2)–O(10)	96.46(6)
O(7)–Na(2)–O(20)	95.3(10)
O(10)–Na(2)–O(1)	91.51(6)
O(13)–Na(2)–O(1)	95.48(6)
O(13)–Na(2)–O(7)	168.72(7)
O(13)–Na(2)–O(10)	76.93(6)
O(13)–Na(2)–O(20)	95.5(10)
O(20)–Na(2)–O(1)	127.2(7)
O(20)–Na(2)–O(10)	141.2(7)

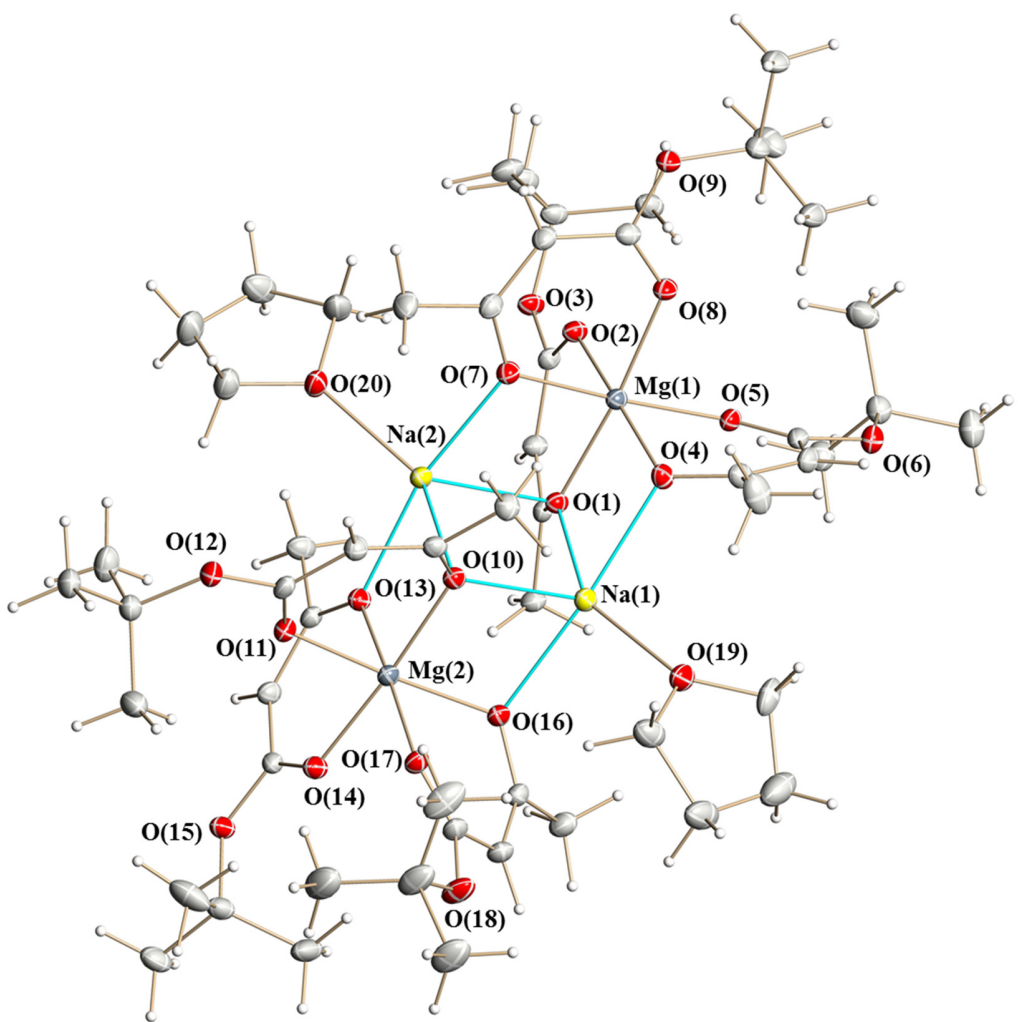


Figure S8. Solid state structure of heterometallic complex $\text{Na}_2\text{Mg}_2(\text{tbaoac})_6(\text{THF})_2$ (4) drawn with thermal ellipsoids at the 40% probability level. Hydrogen atoms are represented by spheres of arbitrary radius. Only metal and oxygen atoms are labeled. The sodium–oxygen bonds to the tbaoac ligands involved in bridging interactions are shown in blue.

Table S13. Selected Bond Distances (Å) and Angles (°) in the Structure of Na₂Mg₂(tbaoc)₂(THF)₂ (**4**)

Bond distances					
Mg(1)–O(1)**	2.0755(17)	Mg(2)–O(10)**	2.0629(17)	Na(1)–O(1)*	2.3943(17)
Mg(1)–O(2)	2.0417(17)	Mg(2)–O(11)	2.0422(18)	Na(1)–O(4)*	2.3546(18)
Mg(1)–O(4)**	2.0387(17)	Mg(2)–O(13)**	2.0429(17)	Na(1)–O(10)*	2.3582(19)
Mg(1)–O(5)	2.0640(18)	Mg(2)–O(14)	2.0418(18)	Na(1)–O(16)*	2.3845(18)
Mg(1)–O(7)**	2.0453(18)	Mg(2)–O(16)**	2.0403(18)	Na(1)–O(19)	2.349(12)
Mg(1)–O(8)	2.0417(17)	Mg(2)–O(17)	2.0721(17)		
Na(2)–O(1)*	2.4479(18)				
Na(2)–O(7)*	2.2859(18)				
Na(2)–O(10)*	2.4149(17)				
Na(2)–O(13)*	2.2876(18)				
Na(2)–O(20)	2.379(11)				
Angles					
O(2)–Mg(1)–O(1)	86.09(7)	O(10)–Mg(2)–O(17)	93.45(7)	O(4)–Na(1)–O(1)	75.32(6)
O(2)–Mg(1)–O(5)	89.76(7)	O(11)–Mg(2)–O(10)	85.85(7)	O(4)–Na(1)–O(10)	103.24(7)
O(2)–Mg(1)–O(7)	91.64(7)	O(11)–Mg(2)–O(13)	89.68(7)	O(4)–Na(1)–O(16)	174.18(7)
O(4)–Mg(1)–O(1)	89.69(7)	O(11)–Mg(2)–O(17)	92.95(7)	O(10)–Na(1)–O(1)	94.74(6)
O(4)–Mg(1)–O(2)	173.66(8)	O(13)–Mg(2)–O(10)	91.40(7)	O(10)–Na(1)–O(16)	74.84(6)
O(4)–Mg(1)–O(5)	85.84(7)	O(13)–Mg(2)–O(17)	174.64(8)	O(16)–Na(1)–O(1)	99.25(6)
O(4)–Mg(1)–O(7)	93.07(7)	O(14)–Mg(2)–O(10)	175.69(8)	O(19)–Na(1)–O(1)	150.3(3)
O(4)–Mg(1)–O(8)	95.95(7)	O(14)–Mg(2)–O(11)	89.89(7)	O(19)–Na(1)–O(4)	88.3(3)
O(5)–Mg(1)–O(1)	94.32(7)	O(14)–Mg(2)–O(13)	87.93(7)	O(19)–Na(1)–O(10)	113.2(3)
O(7)–Mg(1)–O(1)	89.69(7)	O(14)–Mg(2)–O(17)	87.41(7)	O(19)–Na(1)–O(16)	97.5(3)
O(7)–Mg(1)–O(5)	175.84(7)	O(16)–Mg(2)–O(10)	89.23(7)		
O(8)–Mg(1)–O(1)	173.73(7)	O(16)–Mg(2)–O(11)	174.64(8)		
O(8)–Mg(1)–O(2)	88.51(7)	O(16)–Mg(2)–O(13)	92.58(7)		
O(8)–Mg(1)–O(5)	88.82(7)	O(16)–Mg(2)–O(14)	95.05(7)		
O(8)–Mg(1)–O(7)	87.30(7)	O(16)–Mg(2)–O(17)	85.20(7)		

* – bridging oxygen; ** – chelating-bridging oxygen

Angles	
O(7)–Na(2)–O(1)	75.66(6)
O(7)–Na(2)–O(10)	95.34(6)
O(7)–Na(2)–O(13)	167.85(7)
O(7)–Na(2)–O(20)	94.0(5)
O(10)–Na(2)–O(1)	91.95(6)
O(13)–Na(2)–O(1)	94.75(6)
O(13)–Na(2)–O(10)	77.29(6)
O(13)–Na(2)–O(20)	97.7(5)
O(20)–Na(2)–O(1)	128.4(4)
O(20)–Na(2)–O(10)	139.7(4)

ATR-IR Spectra of Heterometallic Precursors

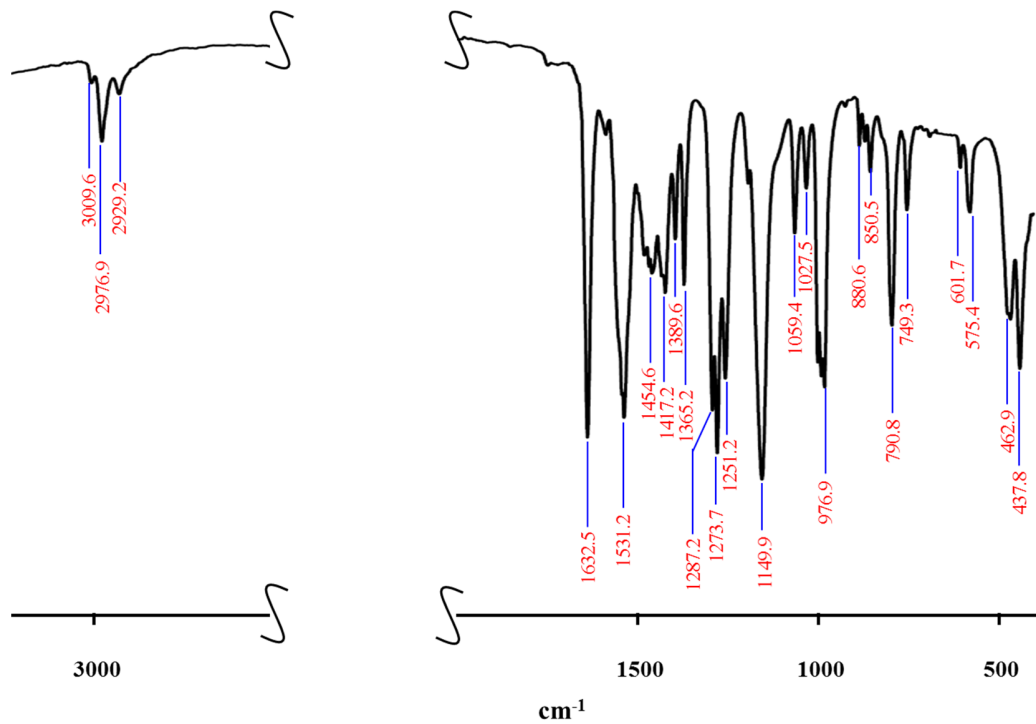


Figure S9. The attenuated total reflection (ATR) spectrum of $\text{Na}_2\text{Fe}_2(\text{tbaoac})_4(\text{THF})_2$ (**1**).

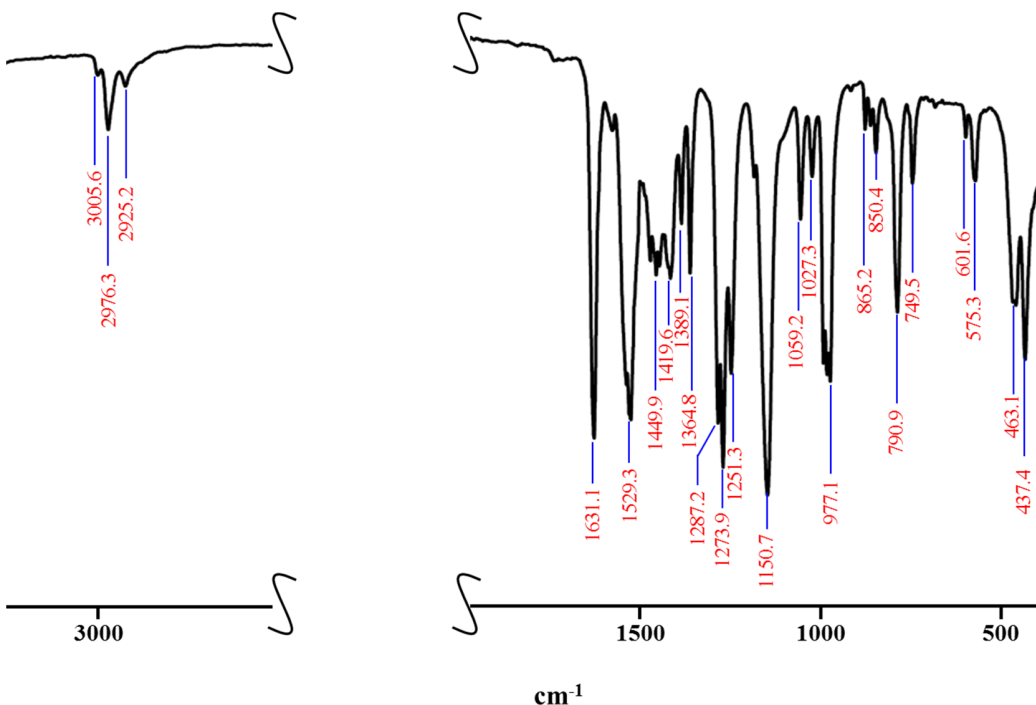


Figure S10. The attenuated total reflection (ATR) spectrum of $\text{Na}_2\text{Co}_2(\text{tbaoac})_4(\text{THF})_2$ (**2**).

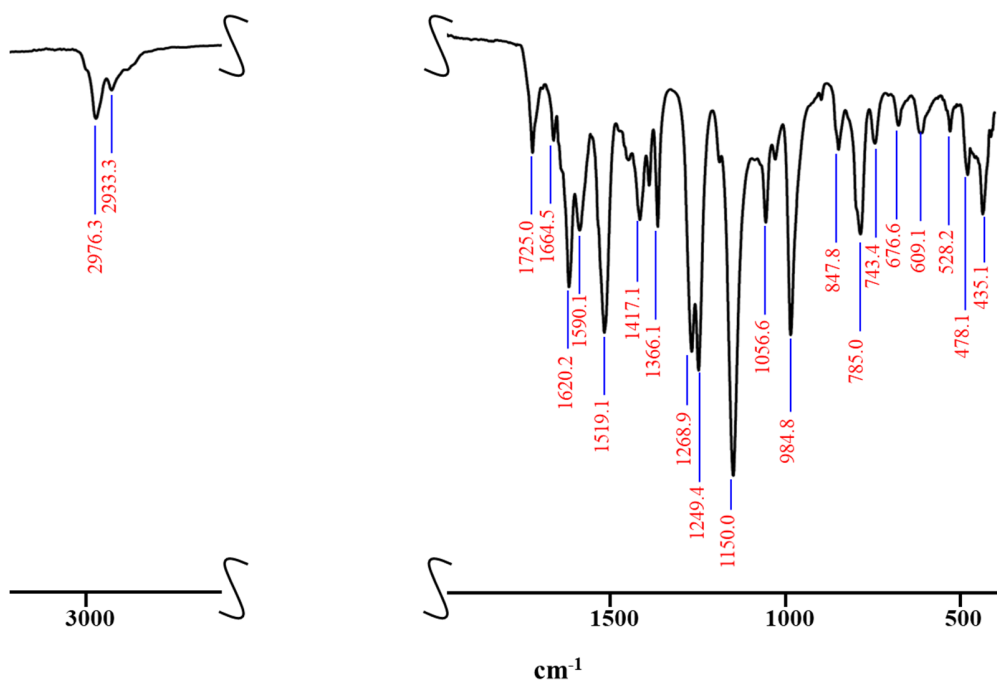


Figure S11. The attenuated total reflection (ATR) spectrum of $\text{Na}_2\text{Ni}_2(\text{tbaoac})_4(\text{THF})_2$ (**3**).

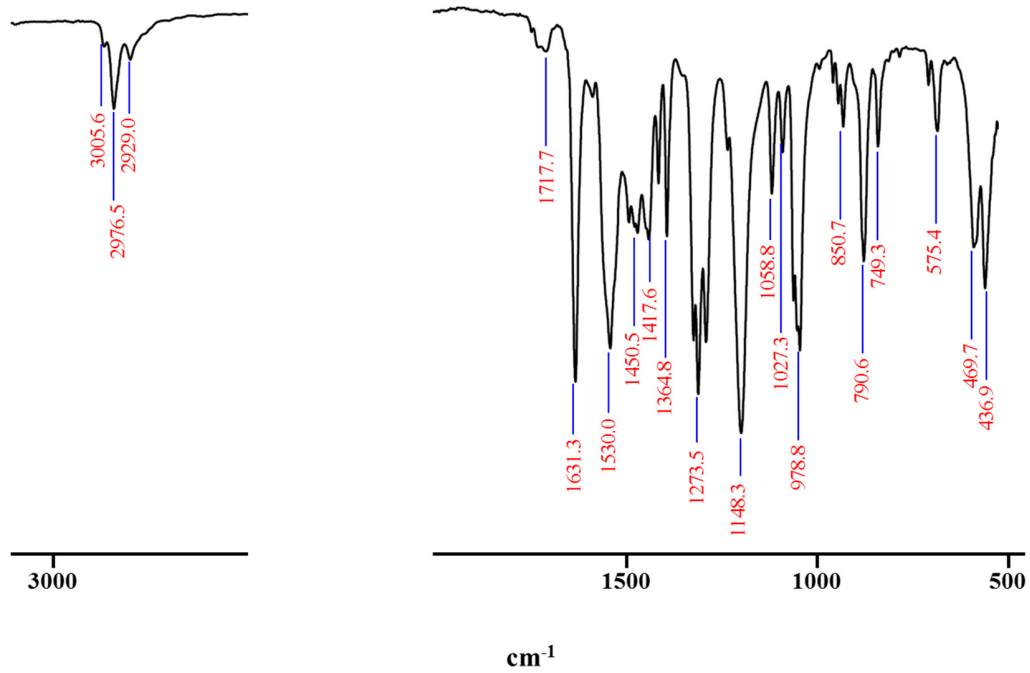


Figure S12. The attenuated total reflection (ATR) spectrum of $\text{Na}_2\text{Mg}_2(\text{tbaoac})_4(\text{THF})_2$ (**4**).

¹H NMR Investigation of Heterometallic Compound Na₂Mg₂(tbaoac)₆(THF)₂ (4)

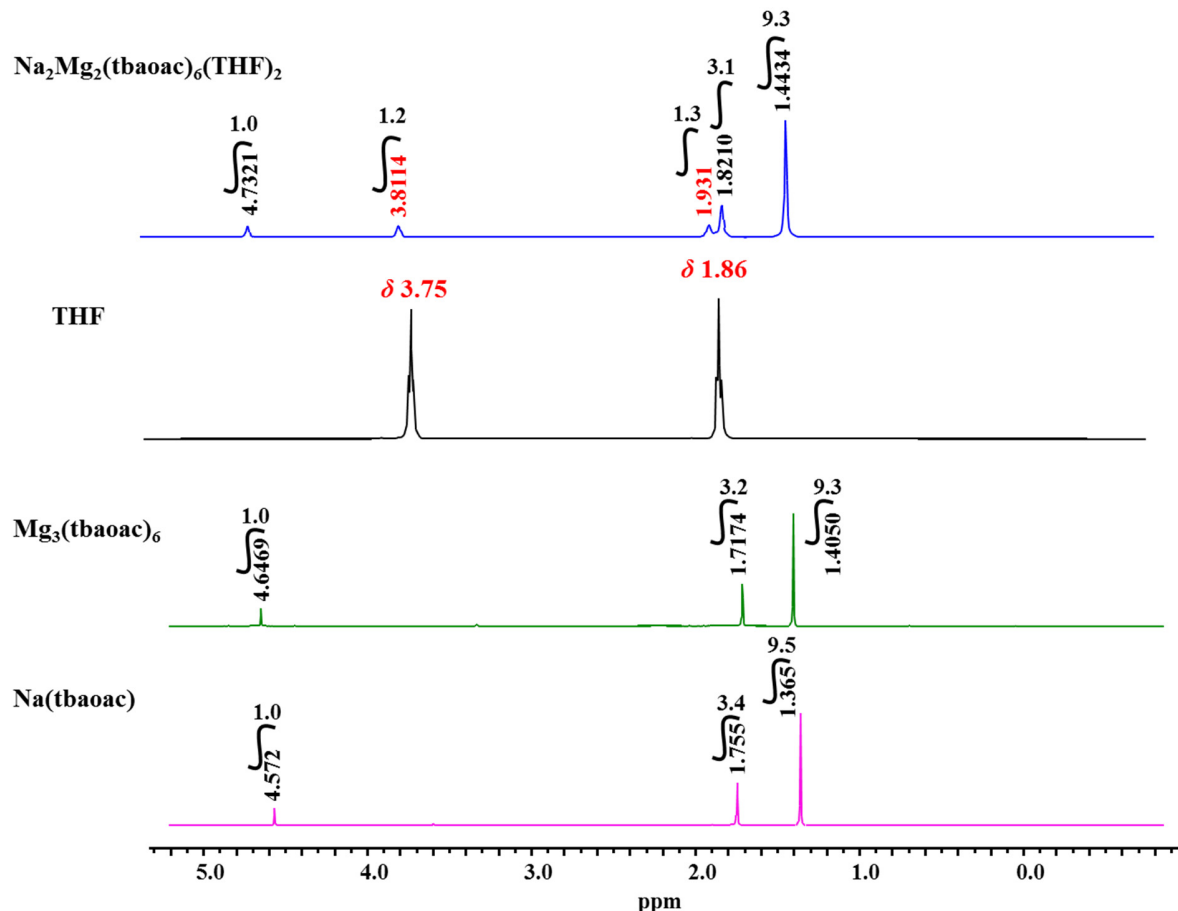


Figure S13. ¹H NMR spectra of Na₂Mg₂(tbaoac)₆(THF)₂ (4) (blue), THF (black), Mg₃(tbaoac)₆ (green), and Na(tbaoac) (pink) in CDCl₃ recorded at room temperature.

Table S14. ¹H NMR Data for Heterometallic Complex Na₂Mg₂(tbaoac)₆(THF)₂ (4)

	THF		tbaoac		
Ligand ratio		1		3	
Proton type	OCH ₂	CH ₂	CH	CH ₃	OC(CH ₃) ₃
Number of protons	4	4	3	9	27
Theoretical ratio	1.3	1.3	1.0	3.0	9.0
Experimental ratio	1.2	1.3	1.0	3.1	9.3

DART Mass Spectra of Heterometallic Precursors

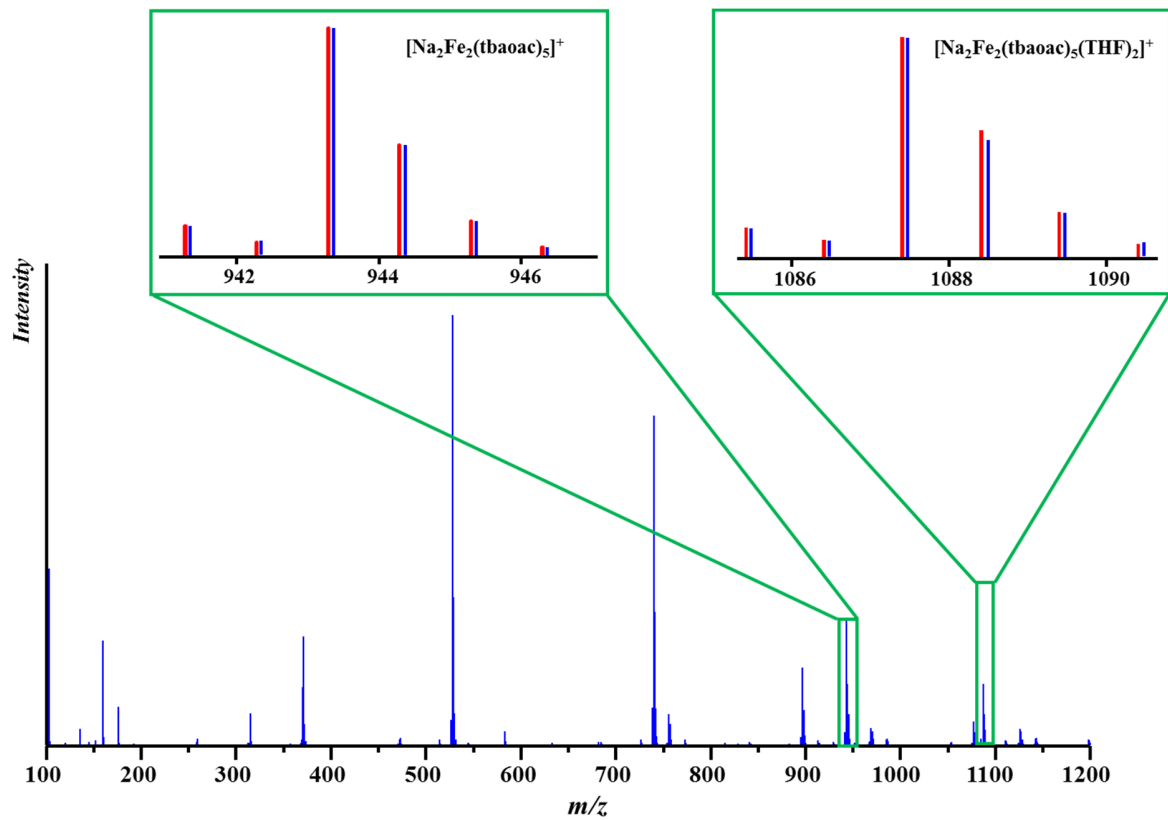


Figure S14. Positive-ion DART mass spectrum of solid $\text{Na}_2\text{Fe}_2(\text{tbaoac})_6(\text{THF})$ (1). The isotope distribution patterns for the $[\text{Na}_2\text{Fe}_2\text{L}_5(\text{THF})_2]^+$ and $[\text{Na}_2\text{Fe}_2\text{L}_5]^+$ ($\text{L} = \text{tbaoac}$) ions are inset (blue and red lines represent experimental and calculated patterns, respectively).

Table S15. Assignment of Ions Detected in the Positive-Ion DART Mass Spectrum of $\text{Na}_2\text{Fe}_2(\text{tbaoc})_6(\text{THF})$ (**1**) ($\text{L} = \text{tbaoc} = \text{C}_8\text{H}_{13}\text{O}_3$)

Ions	Measured, m/z	Calculated, m/z	Δ	% Base
$[\text{Na}_2\text{Fe}_2\text{L}_5(\text{THF})_2]^+$	1087.4007	1087.3971	0.0036	14.4
$[\text{Na}_2\text{Fe}_2\text{L}_5]^+$	943.2837	943.2820	0.0017	29.4
$[\text{NaFe}_2\text{L}_4(\text{THF})_2]^+$	907.3213	907.3208	0.0005	1.3
$[\text{Fe}_2\text{L}_4+\text{H}]^+$	741.2249	741.2237	0.0012	100
$[\text{Fe}_2\text{L}_3]^+$	583.1284	583.1294	-0.0010	3.4
$[\text{FeL}_2(\text{THF})_2+\text{H}]^+$	515.2314	515.2308	0.0006	1.1
$[\text{FeL}_2+\text{H}]^+$	371.1152	371.1157	-0.0005	25.4
$[\text{L}+2\text{H}]^+$	159.1011	159.1021	-0.0010	24.3

Table S16. Assignment of $[\text{Na}_2\text{Fe}_2(\text{tbaoc})_5(\text{THF})_2]^+$ Ions Detected in Positive-Ion DART Mass Spectrum of Solid $\text{Na}_2\text{Fe}_2(\text{tbaoc})_6(\text{THF})_2$ (**1**)

Measured, m/z	Calculated, m/z	Experimental Abundance (%)	Theoretical Abundance (%)	Δ
1085.4069	1085.4015	11.8	12.5	0.0054
1086.4099	1086.4048	5.8	7.0	0.0051
1087.4007	1087.3971	100	100	0.0036
1088.4055	1088.4001	60.2	57.3	0.0054
1089.4087	1089.4026	18.4	20.3	0.0061
1090.4099	1090.4051	3.8	5.3	0.0048

Table S17. Assignment of $[\text{Na}_2\text{Fe}_2(\text{tbaoc})_5]^+$ Ions Detected in Positive-Ion DART Mass Spectrum of Solid $\text{Na}_2\text{Fe}_2(\text{tbaoc})_6(\text{THF})_2$ (**1**)

Measured, m/z	Calculated, m/z	Experimental Abundance (%)	Theoretical Abundance (%)	Δ
941.2901	941.2865	11.8	12.6	0.0036
942.2914	942.2897	6.1	5.9	0.0017
943.2837	943.2820	100	100	0.0017
944.2891	944.2850	47.3	48.7	0.0041
945.2922	945.2874	13.5	15.3	0.0048
946.2955	946.2898	2.4	3.6	0.0057

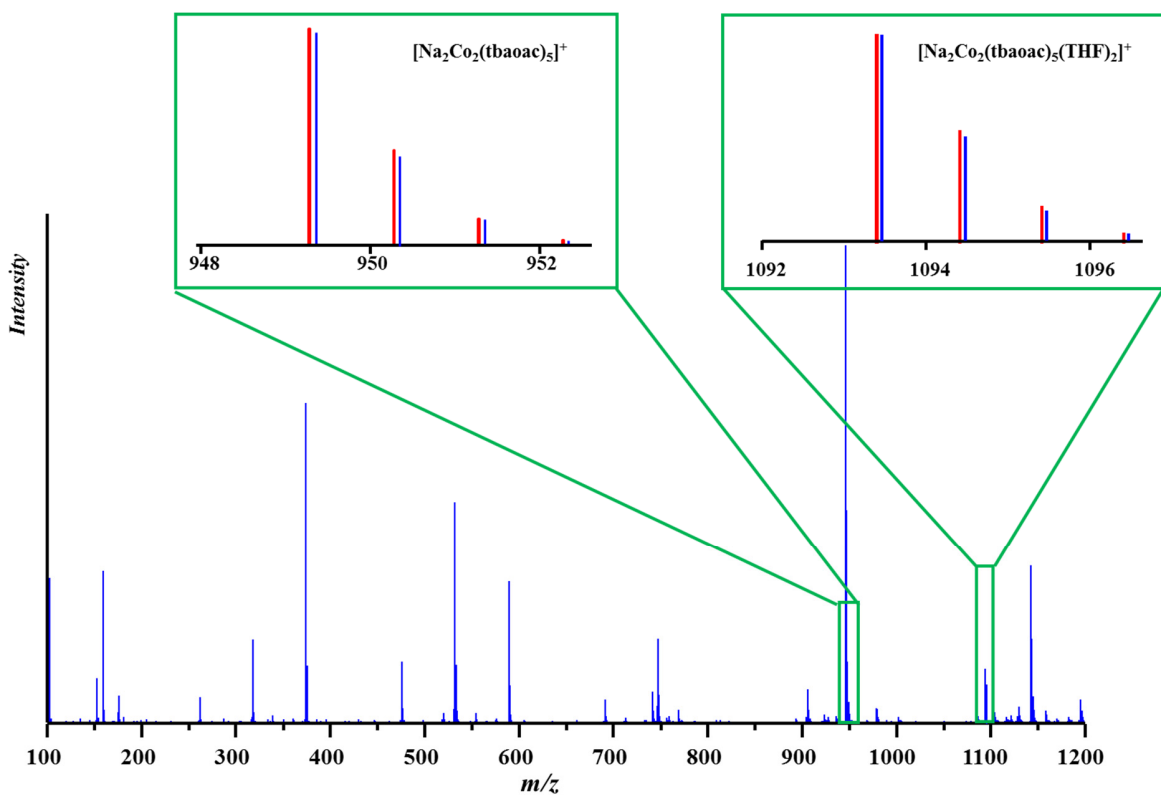


Figure S15. Positive-ion DART mass spectrum of solid $\text{Na}_2\text{Co}_2(\text{tbaoac})_6(\text{THF})$ (**2**). The isotope distribution patterns for the $[\text{Na}_2\text{Co}_2\text{L}_5(\text{THF})_2]^+$ and $[\text{Na}_2\text{Co}_2\text{L}_5]^+$ ($\text{L} = \text{tbaoac}$) ions are inset (blue and red lines represent experimental and calculated patterns, respectively).

Table S18. Assignment of Ions Detected in the Positive-Ion DART Mass Spectrum of $\text{Na}_2\text{Co}_2(\text{tbaoac})_6(\text{THF})$ (**2**) ($\text{L} = \text{tbaoac} = \text{C}_8\text{H}_{13}\text{O}_3$)

Ions	Measured, m/z	Calculated, m/z	Δ	% Base
$[\text{Na}_3\text{Co}_2\text{L}_6]^+$	1129.3586	1129.3545	0.0041	3.3
$[\text{Na}_2\text{Co}_2\text{L}_5(\text{THF})_2]^+$	1093.3955	1093.3933	0.0022	11.2
$[\text{Na}_2\text{Ni}_2\text{L}_5]^+$	949.2810	949.2783	0.0027	100
$[\text{NaCo}_2\text{L}_5+\text{H}]^+$	927.2979	927.2963	0.0016	1.0
$[\text{NaCo}_2\text{L}_4(\text{THF})_2]^+$	913.3184	913.3171	0.0013	1.0
$[\text{NaCo}_2\text{L}_4]^+$	767.2089	769.2021	0.0068	2.6
$[\text{Co}_2\text{L}_4+\text{H}]^+$	747.2242	747.2201	0.0041	17.4
$[\text{Co}_2\text{L}_3]^+$	589.1252	589.1258	-0.0006	29.4
$[\text{NaCoL}_3+\text{H}]^+$	554.1943	554.1902	0.0041	2.0
$[\text{CoL}_2(\text{THF})_2+\text{H}]^+$	518.2324	518.2290	0.0034	1.0
$[\text{NiL}_2+\text{H}]^+$	374.1139	374.1140	-0.0001	66.9
$[\text{L}+2\text{H}]^+$	159.1019	159.1021	-0.0003	31.6

Table S19. Assignment of $[\text{Na}_2\text{Co}_2(\text{tbaoac})_5(\text{THF})_2]^+$ Ions Detected in Positive-Ion DART Mass Spectrum of Solid $\text{Na}_2\text{Co}_2(\text{tbaoac})_6(\text{THF})_2$ (**2**)

Measured, m/z	Calculated, m/z	Experimental Abundance (%)	Theoretical Abundance (%)	Δ
1093.3955	1093.3933	100	100	0.0022
1094.3991	1094.3967	51.8	53.5	0.0024
1095.4014	1095.3996	15.1	17.5	0.0018
1096.4056	1096.4024	3.9	4.3	0.0032

Table S20. Assignment of $[\text{Na}_2\text{Co}_2(\text{tbaoac})_5]^+$ Ions Detected in Positive-Ion DART Mass Spectrum of Solid $\text{Na}_2\text{Co}_2(\text{tbaoac})_6(\text{THF})_2$ (**2**)

Measured, m/z	Calculated, m/z	Experimental Abundance (%)	Theoretical Abundance (%)	Δ
949.2810	949.2783	100	100	0.0027
950.2853	950.2817	39.5	44.6	0.0036
951.2879	951.2845	10.7	12.8	0.0034
952.2907	952.2872	1.9	2.7	0.0025

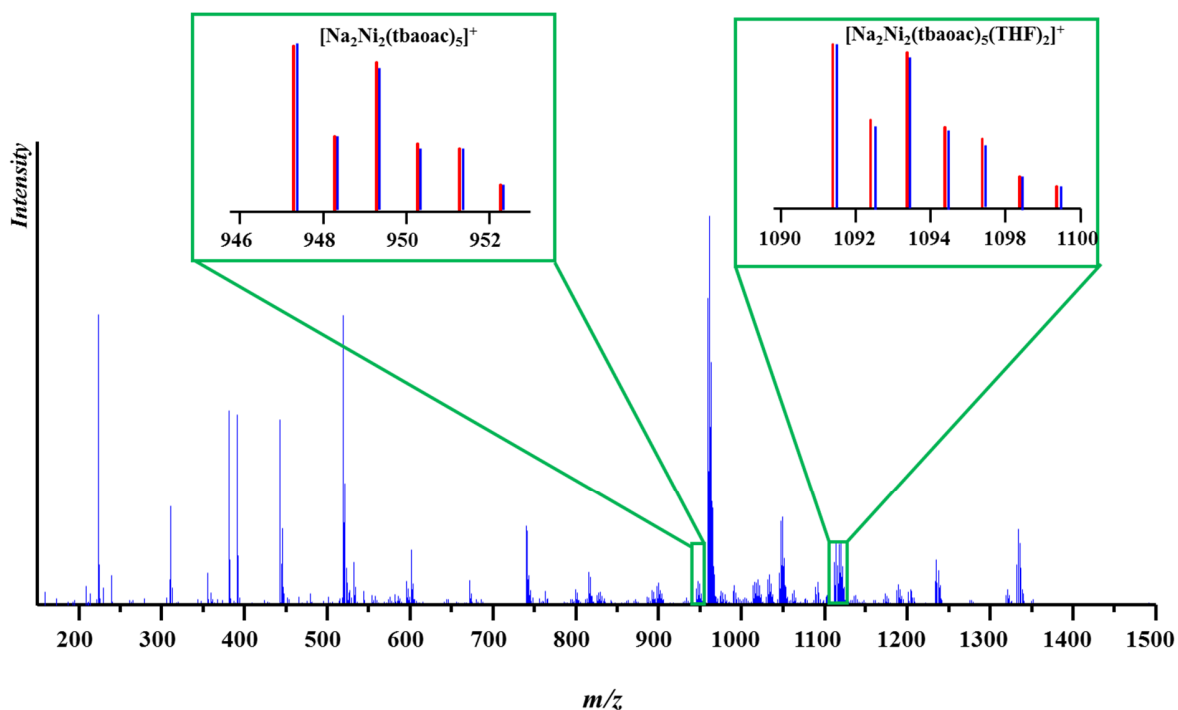


Figure S16. Positive-ion DART mass spectrum of solid $\text{Na}_2\text{Ni}_2(\text{tbaoac})_6(\text{THF})$ (**3**). The isotope distribution patterns for the $[\text{Na}_2\text{Ni}_2\text{L}_5(\text{THF})_2]^+$ and $[\text{Na}_2\text{Ni}_2\text{L}_5]^+$ ($\text{L} = \text{tbaoac}$) ions are inset (blue and red lines represent experimental and calculated patterns, respectively).

Table S21. Assignment of Ions Detected in the Positive-Ion DART Mass Spectrum of $\text{Na}_2\text{Ni}_2(\text{tbaoac})_6(\text{THF})$ (**3**) ($\text{L} = \text{tbaoac} = \text{C}_8\text{H}_{13}\text{O}_3$)

Ions	Measured, m/z	Calculated, m/z	Δ	% Base
$[\text{Na}_3\text{Ni}_2\text{L}_6]^+$	1127.3598	1127.3588	0.0010	1.1
$[\text{Na}_2\text{Ni}_2\text{L}_6+\text{H}]^+$	1105.3793	1105.3769	0.0024	2.5
$[\text{Na}_2\text{Ni}_2\text{L}_5(\text{THF})_2]^+$	1091.3992	1091.3976	0.0016	6.2
$[\text{Na}_2\text{Ni}_2\text{L}_5]^+$	947.2886	947.2826	0.0060	6.3
$[\text{NaNi}_2\text{L}_5+\text{H}]^+$	925.3061	925.3006	0.0055	1.0
$[\text{NaNi}_2\text{L}_4(\text{THF})_2]^+$	911.3247	911.3214	0.0033	1.0
$[\text{NaNi}_2\text{L}_4]^+$	767.2099	767.2063	0.0036	1.1
$[\text{Ni}_2\text{L}_4+\text{H}]^+$	745.2298	745.2244	0.0054	4.2
$[\text{NaNiL}_3+\text{H}]^+$	553.1987	553.1924	0.0063	2.8
$[\text{NiL}_2(\text{THF})_2+\text{H}]^+$	517.2369	517.2311	0.0048	78.1
$[\text{NiL}_2+\text{H}]^+$	373.1193	373.1161	0.0032	1.5
$[\text{L}+2\text{H}]^+$	159.1032	159.1021	0.0011	2.3

Table S22. Assignment of $[\text{Na}_2\text{Ni}_2(\text{tbaoac})_5(\text{THF})_2]^+$ Ions Detected in Positive-Ion DART Mass Spectrum of Solid $\text{Na}_2\text{Ni}_2(\text{tbaoac})_6(\text{THF})_2$ (**3**)

Measured, m/z	Calculated, m/z	Experimental Abundance (%)	Theoretical Abundance (%)	Δ
1091.3992	1091.3976	100	100	0.0016
1092.4059	1092.4010	51.2	53.5	0.0049
1093.4001	1093.3951	89.7	94.6	0.0050
1094.4028	1094.3972	46.0	48.8	0.0056
1095.3975	1095.3934	38.4	41.6	0.0041
1096.4000	1096.3945	19.1	19.0	0.0055
1097.3977	1097.3918	10.8	12.8	0.0059

Table S23. Assignment of $[\text{Na}_2\text{Ni}_2(\text{tbaoac})_5]^+$ Ions Detected in Positive-Ion DART Mass Spectrum of Solid $\text{Na}_2\text{Ni}_2(\text{tbaoac})_6(\text{THF})_2$ (**3**)

Measured, m/z	Calculated, m/z	Experimental Abundance (%)	Theoretical Abundance (%)	Δ
947.2886	947.2826	100	100	0.0060
948.2911	948.2860	45.4	44.6	0.0051
949.2841	949.2796	84.0	89.8	0.0045
950.2869	950.2819	36.7	40.4	0.0050
951.2814	951.2775	37.4	37.3	0.0039
952.2845	952.2790	14.7	15.3	0.0055

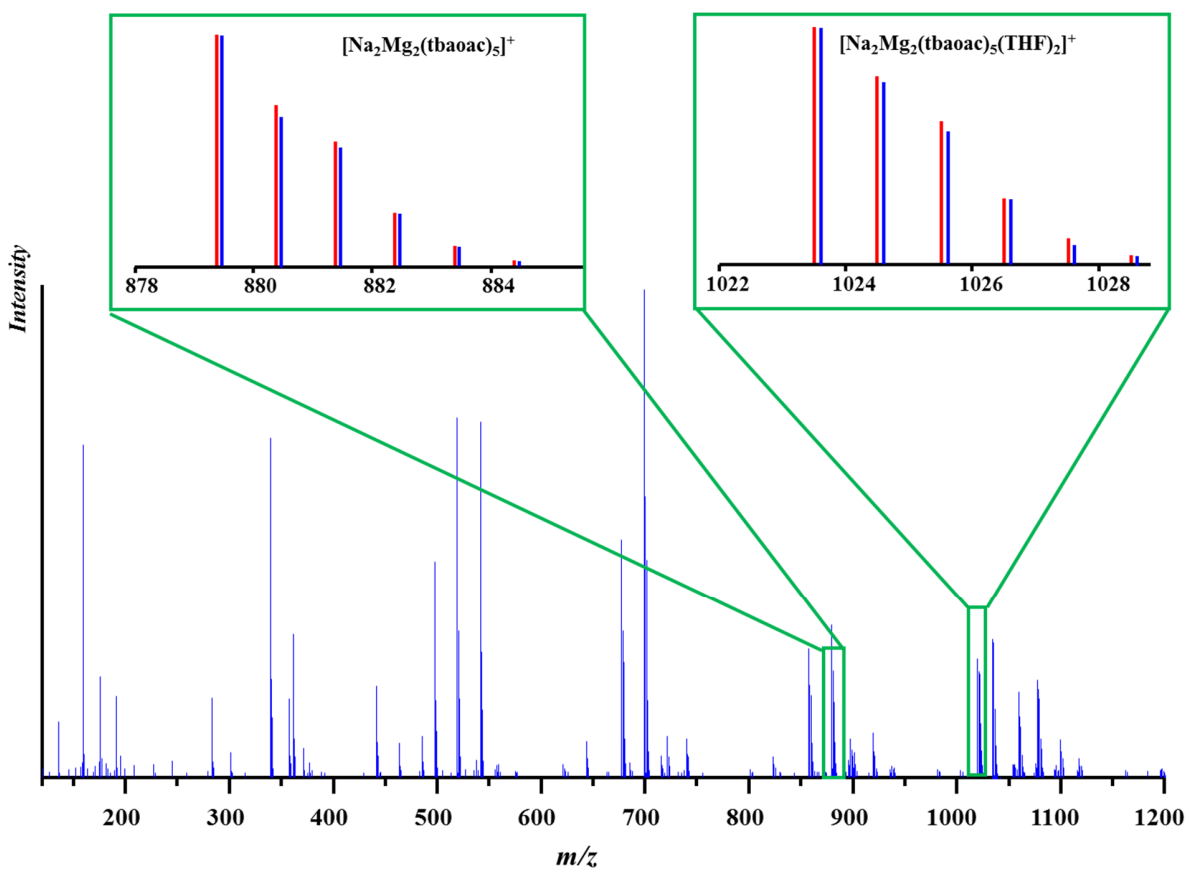


Figure S17. Positive-ion DART mass spectrum of solid $\text{Na}_2\text{Mg}_2(\text{tbaoac})_6(\text{THF})$ (**4**). The isotope distribution patterns for the $[\text{Na}_2\text{Mg}_2\text{L}_5(\text{THF})_2]^+$ and $[\text{Na}_2\text{Mg}_2\text{L}_5]^+$ ($\text{L} = \text{tbaoac}$) ions are inset (blue and red lines represent experimental and calculated patterns, respectively).

Table S24. Assignment of Ions Detected in the Positive-Ion DART Mass Spectrum of $\text{Na}_2\text{Mg}_2(\text{tbaoac})_6(\text{THF})$ (**4**) ($\text{L} = \text{tbaoac} = \text{C}_8\text{H}_{13}\text{O}_3$)

Ions	Measured, m/z	Calculated, m/z	Δ	% Base
$[\text{Na}_2\text{Mg}_2\text{L}_6(\text{THF})_2+\text{H}]^+$	1203.5757	1203.5732	0.0025	1.1
$[\text{Na}_3\text{Mg}_2\text{L}_6]^+$	1059.4613	1059.4582	0.0031	17.5
$[\text{Na}_2\text{Mg}_2\text{L}_6+\text{H}]^+$	1037.4792	1037.4763	0.0029	36.4
$[\text{Na}_2\text{Mg}_2\text{L}_5(\text{THF})_2]^+$	1023.4994	1023.4970	0.0024	26.7
$[\text{Na}_2\text{Mg}_2\text{L}_5]^+$	879.3847	879.3820	0.0027	31.3
$[\text{NaMg}_2\text{L}_5+\text{H}]^+$	857.3992	857.4003	-0.0011	26.4
$[\text{NaMg}_2\text{L}_4(\text{THF})_2]^+$	843.4246	843.4208	0.0038	1.0
$[\text{NaMg}_2\text{L}_4]^+$	699.3035	699.3057	-0.0022	100
$[\text{Mg}_2\text{L}_4+\text{H}]^+$	677.3204	677.3238	-0.0034	48.8
$[\text{NaMg}_2\text{L}_3(\text{THF})_2+\text{H}]^+$	663.3594	663.3571	0.0023	1.4
$[\text{NaMg}_2\text{L}_3+\text{H}]^+$	519.2390	519.2420	-0.0030	73.7
$[\text{Mg}_2\text{L}_2(\text{THF})_2+\text{H}]^+$	483.2784	483.2808	0.0024	1.5
$[\text{Mg}_2\text{L}_2+\text{H}]^+$	339.1626	339.1658	-0.0032	69.7
$[\text{Mg}_2\text{L}]^+$	181.0688	181.0715	-0.0027	2.9
$[\text{L}+2\text{H}]^+$	159.1001	159.1021	-0.0020	68.3

Table S25. Assignment of $[\text{Na}_2\text{Mg}_2(\text{tbaoac})_5(\text{THF})_2]^+$ Ions Detected in Positive-Ion DART Mass Spectrum of Solid $\text{Na}_2\text{Mg}_2(\text{tbaoac})_6(\text{THF})_2$ (**4**)

Measured, m/z	Calculated, m/z	Experimental Abundance (%)	Theoretical Abundance (%)	Δ
1023.4994	1023.4970	100	100	0.0024
1024.5007	1024.4996	72.5	78.8	0.0011
1025.5018	1025.4987	55.0	60.5	0.0031
1026.5053	1026.5000	28.1	28.0	0.0053
1027.5062	1027.5002	9.7	10.9	0.0060
1028.5073	1028.5015	3.4	3.3	0.0058

Table S26. Assignment of $[\text{Na}_2\text{Mg}_2(\text{tbaoac})_5]^+$ Ions Detected in Positive-Ion DART Mass Spectrum of Solid $\text{Na}_2\text{Mg}_2(\text{tbaoac})_6(\text{THF})_2$ (**4**)

Measured, m/z	Calculated, m/z	Experimental Abundance (%)	Theoretical Abundance (%)	Δ
879.3847	879.3820	100	100	0.0027
880.3879	880.3844	64.2	69.9	0.0035
881.3860	881.3831	52.3	53.6	0.0029
882.3882	882.3845	22.9	22.7	0.0037
883.3892	883.3844	8.6	8.5	0.0048
884.3908	884.3858	1.9	2.3	0.0050

Thermogravimetric Analysis (TGA) of Heterometallic Precursors

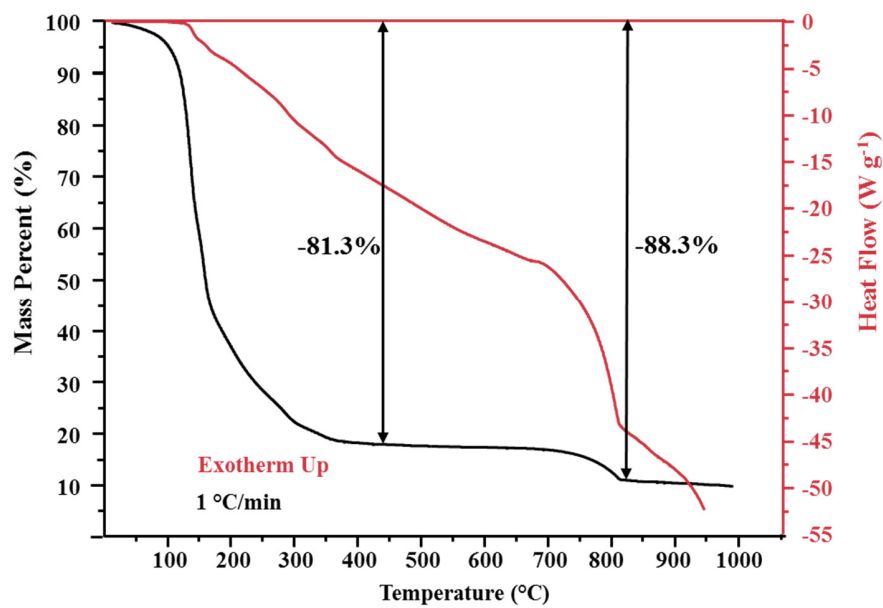


Figure 18. TGA diagram of heterometallic precursor $\text{Na}_2\text{Fe}_2(\text{tbaoac})_6(\text{THF})_2$ (**1**) recorded under air at the heating rate of $1\text{ }^{\circ}\text{C}/\text{min}$.

Thermal Decomposition of Heterometallic Precursors

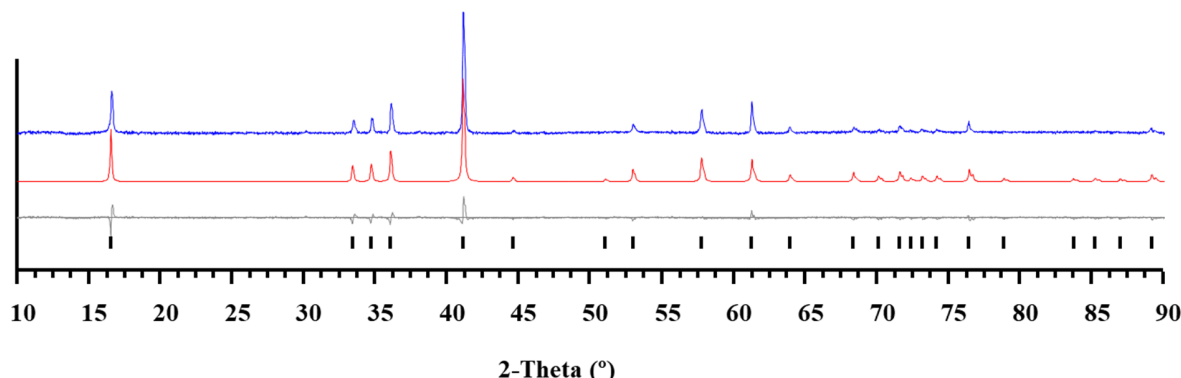


Figure S19. X-ray powder diffraction pattern of $\alpha(\text{O}3)$ -NaFeO₂ obtained by thermal decomposition of heterometallic precursor Na₂Fe₂(tbaoac)₆(THF)₂ (**1**) at 450 °C in the O₂ atmosphere and the Le Bail fit. Blue and red curves are experimental and calculated patterns, respectively. Grey curve is the difference line with theoretical peak positions shown at the bottom.

Table S27. Comparison of the Unit Cell Parameters for $\alpha(\text{O}3)$ -type NaFeO₂ Oxide Obtained by Thermal Decomposition of Heterometallic Precursor Na₂Fe₂(tbaoac)₆(THF)₂ (**1**) at 450 °C in the O₂ Atmosphere with the Literature Data

$\alpha(\text{O}3)$ -type NaFeO ₂		
	Le Bail fit data	Literature data ⁹
Space Group		<i>R</i> -3 <i>m</i>
<i>a</i> (Å)	3.0201(1)	3.026 ^a
<i>c</i> (Å)	16.0954(1)	16.10 ^a

^a No standard deviations were reported.

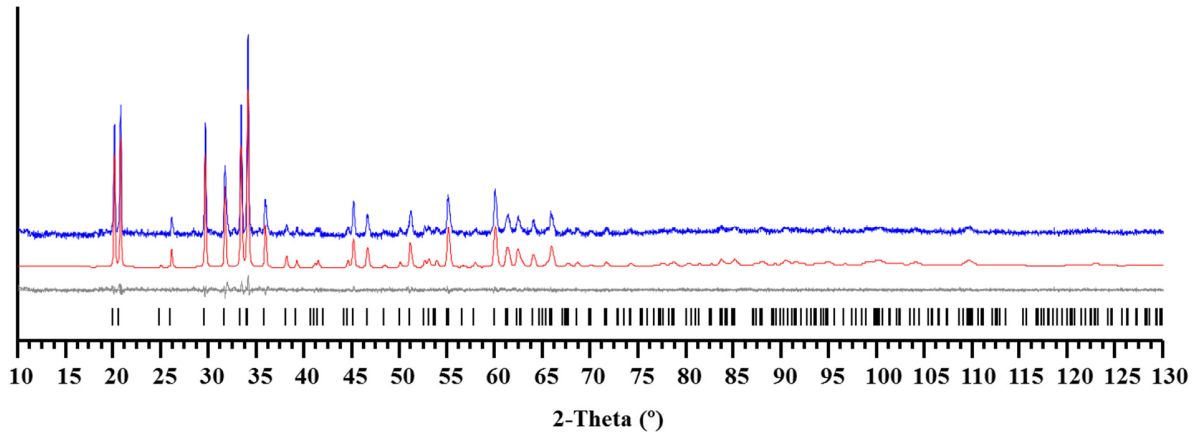


Figure S20. X-ray powder diffraction pattern of β -NaFeO₂ obtained by thermal decomposition of heterometallic precursor Na₂Fe₂(tbaoac)₆(THF)₂ (**1**) at 500 °C in the air and the Le Bail fit. Blue and red curves are experimental and calculated patterns, respectively. Grey curve is the difference line with theoretical peak positions shown at the bottom.

Table S28. Comparison of the Unit Cell Parameters for β -type NaFeO₂ Oxide Obtained by Thermal Decomposition of Heterometallic Precursor Na₂Fe₂(tbaoac)₆(THF)₂ (**1**) at 500 °C in the Air with the Literature Data

β -NaFeO ₂		
	Le Bail fit data	Literature data ¹⁰
Space Group		<i>Pna</i> 2 ₁
<i>a</i> (Å)	5.6569(1)	5.672(2)
<i>b</i> (Å)	7.1515(1)	7.136(2)
<i>c</i> (Å)	5.3797(1)	5.377(2)

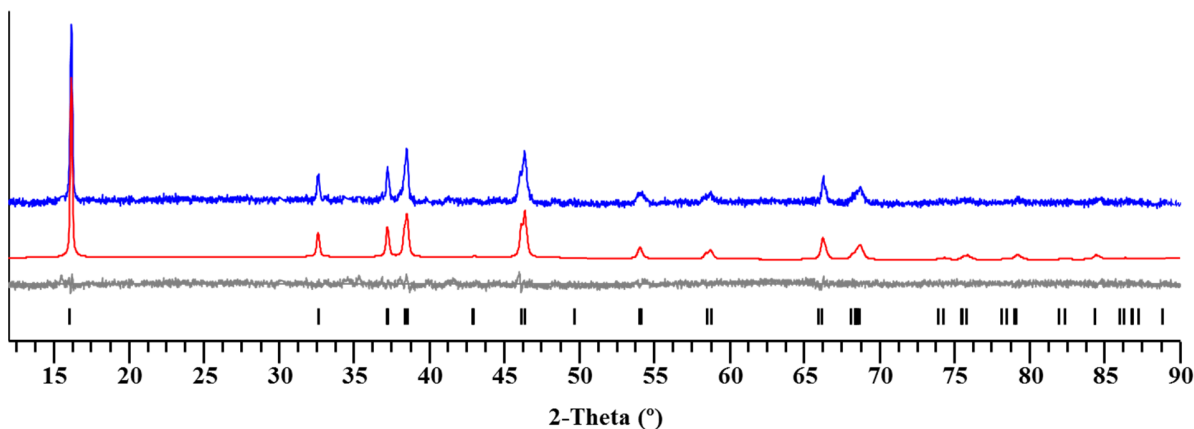


Figure S21. X-ray powder diffraction pattern of O'3-type $\text{Na}_{0.81}\text{CoO}_2$ obtained by thermal decomposition of heterometallic precursor $\text{Na}_2\text{Co}_2(\text{tbaoac})_6(\text{THF})_2$ (**2**) at 450 °C and the Le Bail fit. Blue and red curves are experimental and calculated patterns, respectively. Grey curve is the difference line with theoretical peak positions shown at the bottom.

Table S29. Comparison of the Unit Cell Parameters for O'3-type $\text{Na}_{0.81}\text{CoO}_2$ Oxide Obtained by Thermal Decomposition of Heterometallic Precursor $\text{Na}_2\text{Co}_2(\text{tbaoac})_6(\text{THF})_2$ (**2**) at 450 °C with the Literature Data.

O'3-type $\text{Na}_{2/3}\text{CoO}_2$		
	Le Bail fit data	Literature data ¹¹
Space Group	$P6_3/mmc$	
a (Å)	4.8874(6)	4.8912 ^a
b (Å)	2.8316(5)	2.8681 ^a
c (Å)	5.7480(5)	5.7937 ^a
β (°)	110.74(1)	111.84 ^a

^a No standard deviations were reported.

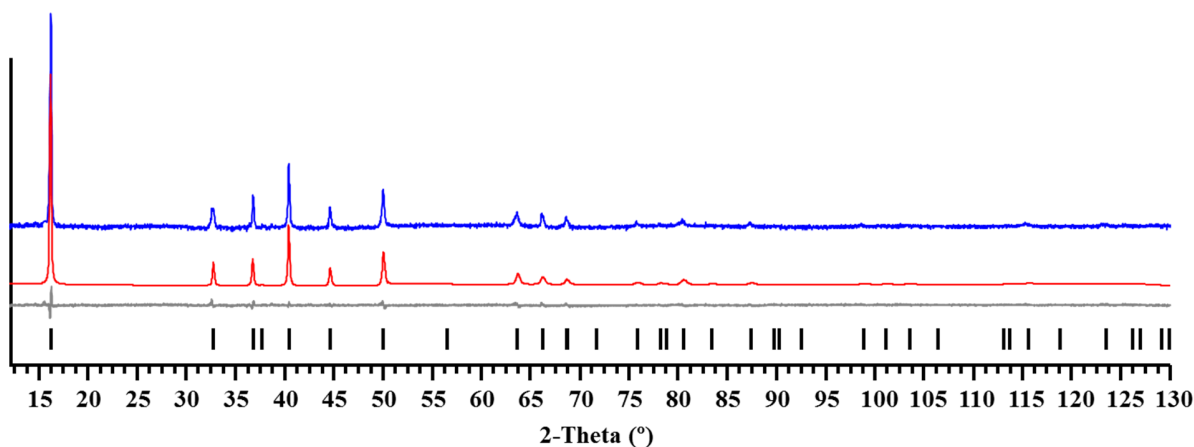


Figure S22. X-ray powder diffraction pattern of P2-type $\text{Na}_{0.70}\text{CoO}_2$ obtained by thermal decomposition of heterometallic precursor $\text{Na}_2\text{Co}_2(\text{tbaoc})_6(\text{THF})_2$ (**2**) at 750 °C and the Le Bail fit. Blue and red curves are experimental and calculated patterns, respectively. Grey curve is the difference line with theoretical peak positions shown at the bottom.

Table S30. Comparison of the Unit Cell Parameters for P2-type $\text{Na}_{0.70}\text{CoO}_2$ Oxide Obtained by Thermal Decomposition of Heterometallic Precursor $\text{Na}_2\text{Co}_2(\text{tbaoc})_6(\text{THF})_2$ (**2**) at 750 °C with the Literature Data.

P2-type $\text{Na}_{2/3}\text{CoO}_2$		
	Le Bail fit data	Literature data ¹¹
Space Group		$P6_3/mmc$
a (Å)	2.82991(11)	2.8320 ^a
c (Å)	10.90346(11)	10.8971 ^a

^aNo standard deviations were reported.

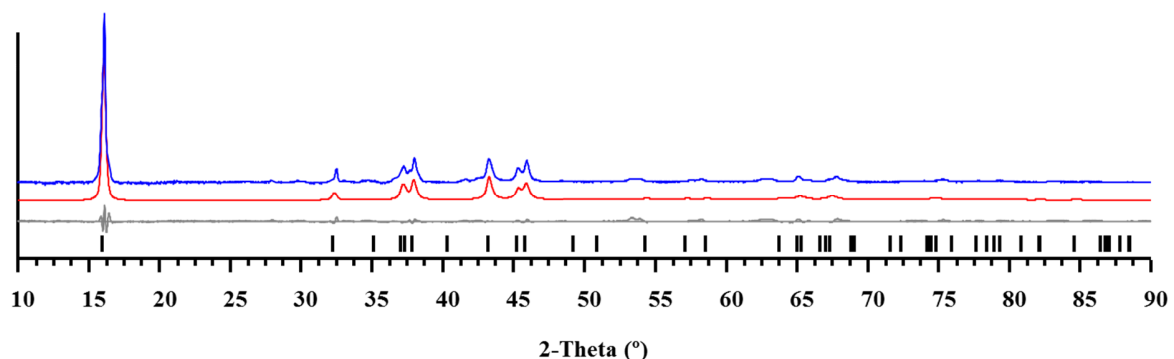


Figure S23. X-ray powder diffraction pattern of O'3-type NaNiO_2 obtained by thermal decomposition of heterometallic precursor $\text{Na}_2\text{Ni}_2(\text{tbaoac})_6(\text{THF})_2$ (**3**) at 600 °C and the Le Bail fit. Blue and red curves are experimental and calculated patterns, respectively. Grey curve is the difference line with theoretical peak positions shown at the bottom.

Table S31. Comparison of the Unit Cell Parameters for O'3-type NaNiO_2 Oxide Obtained by Thermal Decomposition of Heterometallic Precursor $\text{Na}_2\text{Ni}_2(\text{tbaoac})_6(\text{THF})_2$ (**3**) at 600 °C with the Literature Data.

O'3-type NaNiO_2		
	Le Bail fit data	Literature data ¹²
Space Group		$C2/m$
a (Å)	5.33485(2)	5.323(4)
b (Å)	2.83401(2)	2.845(2)
c (Å)	5.60863(2)	5.583(5)
β (°)	109.912(1)	110.44(4)

TEM Image of Sodium Cobalt Oxide and Its Electrochemical Behavior

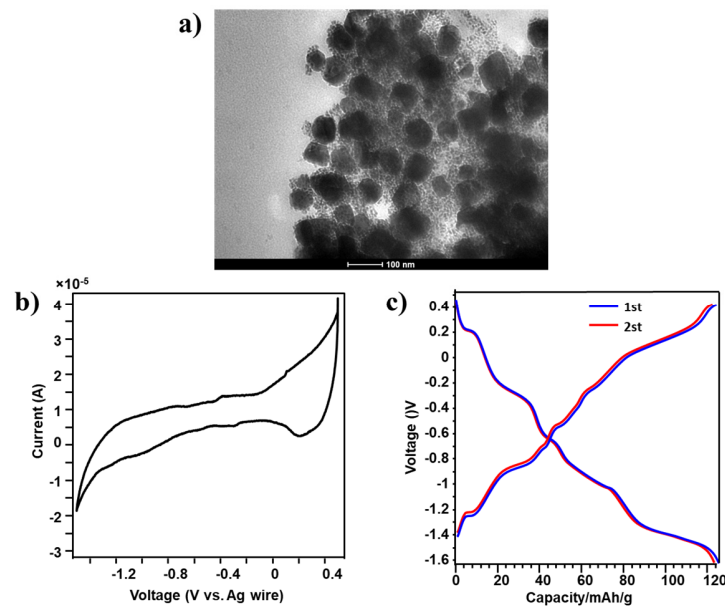


Figure S24. (a) TEM image of P2- $\text{Na}_{2/3}\text{CoO}_2$; (b) Cyclic voltammetry of P2- $\text{Na}_{2/3}\text{CoO}_2$ against Ag wire ($\text{Ag}^+/\text{Ag} = 0.79$ V and $\text{Na}^+/\text{Na} = -2.71$ V); (c) Galvanostatic discharge profile of P2- $\text{Na}_{2/3}\text{CoO}_2$ (blue and red curves are the 1st and 2nd scans, respectively).

References

1. H. Han, Z. Wei, M. C. Barry, J. C. Carozza, M. Alkan, A. Y. Rogachev, A. S. Filatov, A. M. Abakumov and E. V. Dikarev, *Chem. Sci.*, 2018, **9**, 4736-4745.
2. H. Han, Z. Wei, M. C. Barry, A. S. Filatov and E. V. Dikarev, *Dalton Trans.*, 2017, **46**, 5644-5649.
3. Z. Wei, H. Han, A. S. Filatov and E. V. Dikarev, *Chem. Sci.*, 2014, **5**, 813-818.
4. SAINT; Part of Bruker APEX3 Software Package: Bruker AXS. **2015**, Version 8.34A.
5. SADABS; Part of Bruker APEX3 Software Package: Bruker AXS. **2015**, Version 2014/5.
6. G. M. Sheldrick, *Acta Crystallogr., Sect. A: Found. Adv.*, 2015, **71**, 3-8.
7. G. M. Sheldrick, *Acta Crystallogr., Sect. C: Struct. Chem.* 2015, **71**, 3-8.
8. O.V. Dolomanov, L.J. Bourhis, R.J. Gildea, J.A.K. Howard, H. Puschmann, *J. Appl. Cryst.* 2009, **42**, 339-341.
9. E. Lee, D. E. Brown, E. E. Alp, Y. Ren, J. Lu, J. Woo and C. S. Johnson, *Chem. Mater.*, 2015, **27**, 6755-6764.
10. D. Kim, S. H. Kang, M. Slater, S. Rood, T. Vaughey John, N. Karan, M. Balasubramanian and S. Johnson Christopher, *Adv. Energy Mater.*, 2011, **1**, 333-336.
11. Y. Lei, X. Li, L. Liu and G. Ceder, *Chem. Mater.*, 2014, **26**, 5288-5296.
12. M. H. Han, E. Gonzalo, M. Casas-Cabanas and T. Rojo, *J. Power Sources*, 2014, **258**, 266-271.